INSTITUTO SUPERIOR TÉCNICO
Universidade Técnica de Lisboa

Toward a fully automatic left ventricle segmentation using cine-MR images

Isabela Maria Montenegro da Silva

Dissertação para obtenção do Grau de Mestre em

Engenharia Biomédica

Júri

Presidente:	Prof.ª Patrícia Figueiredo
Orientador:	Prof. João Sanches
Orientador:	Prof.ª Ana G. Almeida
Vogal:	Doutor Jacinto Nascimento

Outubro 2008

Aos meus pais e ao meu irmão

Acknowledgments

Em primeiro lugar, gostaria de agradecer ao Prof. João Sanches por ter abraçado este projecto desde que o apresentei e por toda a dedicação e apoio que me deu ao longo deste trabalho. Gostaria também de agradecer à Prof. Ana G. Almeida em especial, e à Sociedade Portuguesa de Ressonancia Magnética e a todos que lá trabalham, pela disponibilidade e apoio, e pela confiança que me permitiu circular com muita facilidade e ter sempre os dados que necessitava.

Já noutro âmbito, gostaria de agradecer a toda a familia e aos meus amigos que me ajudaram neste percurso e que acreditaram sempre em mim.

Abstract

Left ventricle (LV) function is assessed by manually segmenting short-axis cardiac *cine magnetic resonance* (cine-MR) images. It is a labor, time-consuming, operator biased task. A series of difficulties arise from these images, that make automatic segmentation of the LV a challenging task: (i) misalignment along the LV volume, (ii) signal intensity variation over the volume and over the slice and (iii) the presence papillary muscles.

In this thesis, the first steps toward a full automatic LV segmentation algorithm based on a single view of the LV are presented:

1. **Automatic crop**: selects a sub-volume containing the LV in all images and in all temporal frames from the acquired data. It is based on three assumptions: (i) the LV is close of the center of the image, (ii) the LV is circular shaped and (iii) there is a high temporal variability of the image intensity in the myocardium boundaries due the heart beat.

2. **Alignment-by-reconstruction**: novel technique to solve the misalignment due to respiratory motion, inspired on the work from Sanches *et al.* [1] in ultrasound;

3. **Segmentation**: The LV is segmented slice by slice using active contours (2D) in an energy minimization formulation with *gradient vector flow* (GVF) as external field. The automatic initialization algorithm here implemented is original, and it is based on the property of intersecting chords.

Preliminary tests with synthetic and real data from 17 patients were performed with successful results.

Keywords: left ventricle, automatic crop, intra-plane alignment, snake initialization.

Resumo

A função do *ventriculo esquerdo* (VE) é estimada através de segmentação manual de imagens cine-RM cardiacas do eixo curto. É uma tarefa trabalhosa, morosa e dependente da experiência do especialista. Estas imagens apresentam uma serie de dificuldades: (i) desalinhamento ao longo do volume, (ii) variação da intensidade do sinal ao longo do volume e ao longo do corte e (iii) presença de músculos papilares.

Neste trabalho são apresentados três primeiros passos para uma completa automatização da segmentação do VE:

1. **Corte automatico**: selecionar um sub-volume contendo o VE em todas as imagens quer no dominio do espaço quer no dominio do tempo. Este algoritmo baseia-se em três hipoteses: (i) o VE está localizado perto do centro da imagem e (ii) tem forma circular, e (iii) existe elevada variabilidade temporal do sinal da imagem na fronteira do miocardio devido ao movimento cardiaco.

2. **Alinhamento-com-reconstrucção**: técnica inovadora que resolve o problema de desalinhamento devido ao movimento respiratorio, inspirado no trabalho de Sanches *et al.* [1] em ultrasom;

3. **Segmentação**: O VE é segmentado corte a corte usando contornos activos (2D) numa formulação de minimização de energia e GVF como campo de energia externa. Foi implementado um algoritmo de inicialização automática da *snake* baseado na propriedade de intersecção de *chords*.

Foram efectuados testes preliminares com dados sintéticos e dados reais de 17 doentes com sucesso.

Palvras-chave: ventriculo esquerdo, corte automatico, alinhamento intra-planos, inicialização da *snake*.

Contents

List of Figures

List of Tables

Abbreviations

n-D+T n-dimensional and time

AHA American Heart Association

BB Bounding box

CT Computed Tomography

CVD Cardiovascular Disease

DICOM Digital Imaging and Communications in Medicine

DM Deformable models

ECG Electrocardiogram

ED End of the diastole

EDV End-Diastolic Volume

EF Ejection Fraction

ES End of the systole

ESF End systolic frame

ESV End-Systolic Volume

FA Flip angle

FOV Field Of View

GVF Gradient Vector Flow

ISR Institute for Systems and Robotics

IST Instituto Superior Técnico

HT Hough Transform

LV Left Ventricle

MIA Medical Image Analysis

MR Magnetic Resonance

MRF Markov random fields

MRI Magnetic Resonance Imaging

PM Papillary muscles

ROI Region Of Interest

SA Short Axis

SPRM Sociedade Portuguesa de Ressonância Magnética

STD Standard Deviation

TE Echo time

TR Repetition time

UTL Universidade Técnica de Lisboa

WHO World Health Organization

Definitions

Apex The apex of the heart is the lowest superficial part of the heart.

Apical An apical plane is set close to the apex.

Basal A basal plane is set close to the base of the ventricle, in opposition to the apex.

Blood-pool Is the cavity containing the blood surrounded by the myocardium.

Chord Segment of a secant line lying inside of the circumference

Diastole Period of the cardiac cycle when the heart fills with blood; Dilation of the heart with muscular relaxation.

Endocardium Is the innermost layer of tissue that lines the chambers of the heart.

Epicardium Describes the outer layer of heart tissue.

Myocardium Is the muscular tissue of the heart.

Pixel In digital imaging, a pixel (picture element) is the smallest piece of information in an image.

Papillary muscles One of the group of myocardial bundles that terminate in the chordae tendineae which attach to the cusps of the atrioventricular valves.

QRS complex The QRS complex is a structure on the ECG that corresponds to the depolarization of the ventricles.

Short Axis Cardiac plane perpendicular to the long axis of the left ventricle that transects the apex and the center of the mitral valve plane.

Stroke also know as heart attack or myocardial infarction, occurs when the blood supply to part of the heart is interrupted.

Systole Period of the cardiac cycle when the heart drives the blood out of the chambers; Contraction of the heart.

Voxel Is a volume element, representing a value on a regular grid in three dimensional space.

Chapter 1

Introduction

Cardiovascular diseases (CVD) include coronary heart disease (heart attack), hypertension, hypertension heart disease, peripheral artery disease, rheumatic heart disease and congenital heart disease. According to *World Health Organization* (WHO), globally they are the leading cause of death: an estimated 17.5 million people died from CVD in 2005, representing 30% of all global deaths [2]. Of these deaths, 43% were due to heart attacks and 33% due to stroke.

Attending to these numbers, there is an increasing demand for technology able to provide qualitative and quantitative information about morphology and function of the heart. Its use can help clinical diagnosis, treatment and follow-up of cardiac diseases.

1.1 Background

There are several non-invasive cardiac imaging techniques available in the clinical routine [3], such as echocardiography, *single photon emission computed tomography* (SPECT), *computed tomography* (CT) and *magnetic resonance imaging* (MRI).

These techniques provide 2-D+T and 3-D+T information with continuously increasing spatial and temporal resolution. Therefore, a single cardiac examination can result in a large amount of data. These advances have led to a raising need for efficient algorithms to automate the extraction of clinical relevant parameters.

MRI is one of the preferred diagnostic technique due to its high spatial resolution, soft-tissue contrast and non-ionizing imaging technique. Furthermore, besides the structural information such as anatomy and tissue characterization, it provides dynamic analysis such as perfusion, metabolism and function measurements in one single examination [4].

MRI is widely used to assess cardiac *left ventricle* (LV) function and diagnose several heart pathologies [5, 6, 7] and it is now considered the "gold standard" to evaluate the LV function [8]. One important parameter used to evaluate it is the *ejection fraction* (EF). The EF is a global index of the LV shortening and is generally considered as one of the most meaningful measures of the LV pump function. It is defined as the ratio of the volume difference between the *end of the diastole* (ED) and the *end of the systole* (ES)

(*end-systolic volume* (ESV)) to the *end-diastolic volume* (EDV):

$$EF = \frac{EDV - ESV}{EDV}. \tag{1.1}$$

To estimate the EF, the physicians have to manually draw the LV internal contour from a stack of *short-axis* (SA) cine-MR images at the ED and ES phases of the cardiac cycles. The SA stacks are usually composed by 10 up to 16 slices and 15 up to 30 time frames are acquired per cardiac cycle, corresponding to different phases of this cycle. Manually processing all this vast amount of data is time consuming and subjective, compromising the accuracy and reproducibility of the quantitative measurements. Therefore, computer assistance is needed. Full automatic LV tracking and segmentation process is complex and still an open problem.

1.2 Left ventricle short axis cine-MR images

The standard MRI protocol for a cardiac patient consists on three main steps: setup, planing and acquisition.

In the setup, the technician prepares the patient. A cardiac coil, used to send and receive radio-frequency signal, is placed over the chest of the patient (see Fig.1.1(a)). The patient has also *electro-cardiogram* (ECG) leds attached. Due to the heart beat, cardiac MR imaging is gated to the ECG so that the images are acquired at the same cardiac phase, minimizing motion artifacts [9]. Motion due to respiration is compensated by acquiring during breath-hold periods. Automatic dual cardiac-respiratory triggering is also possible but it is still an under-development technique [10]. In Fig.1.1(b) it is possible to observe the triggering at the same phase of the cardiac cycle and the silent periods at a phase of the respiratory cycle.

(a) Philips SENSE Cardiac coil 6 elements

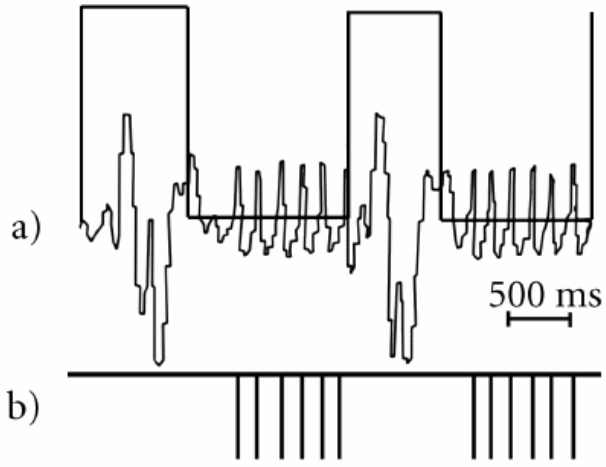

(b) Dual cardiac-respiratory triggering. a) Acquisition window from two respiratory cycles and ECG b) Trigger pulses sent to MRI console based on cardiac cycle [11]

Figure 1.1: Cardiac MRI protocol: setup.

The examination table is moved toward placing the heart on the iso-center of the magnet (Fig.1.2(a)), where the homogeneity of the magnetic field is higher. Therefore, higher image quality is achieved.

When the preparation of the patient is finished, the technicians and physicians start the cardiac exam in a contiguous room: first, a set of low resolution images are acquired to locate the heart and design the exam (planing step). Then, the required images for the diagnose are acquired in the cardiac planes as defined by the *American Heart Association* (AHA) [12] (see Fig.1.2(b)): the referred SA cine-MR images are acquired in a plane perpendicular to the long axis of the heart.

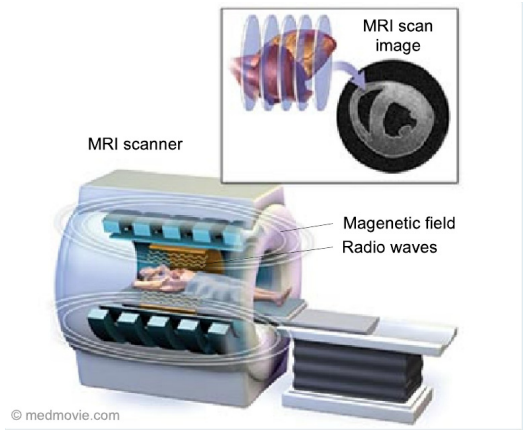

(a) MRI *scanner* (image from *www.medmovie.com*)

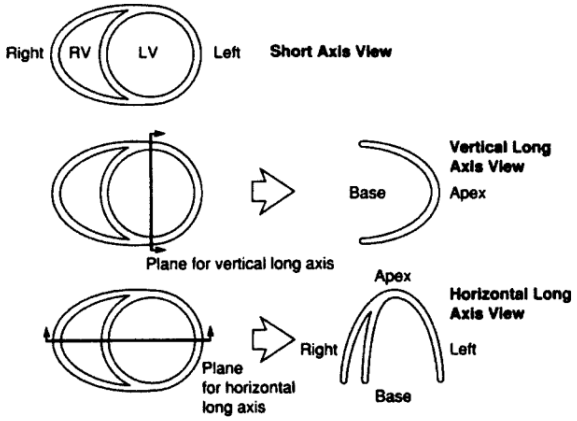

(b) Cardiac plane definition according to the AHA [12]

Figure 1.2: Cardiac MRI protocol: planning.

In MRI, the image intensity represents the radio-frequency signal amplitude and depends on the imaging sequence. In LV function studies, gradient-echo based sequences are preferred [13] due to their greater speed, resulting in bright-blood images. Recently, cine-MR using steady state free precession is used routinely. This imaging sequence provides higher contrast between muscle and blood, also resulting in bright-blood images. Normally no contrast agent is required. An example of a sequence of images to study the LV function is presented in Fig.1.3. A series of difficulties arise from these SA cine-MR images, that make automatic segmentation of the LV a challenging task:

1. During suspended respiration, there is a displacement of the diaphragm and the heart does not return to the same position on consecutive heart beats [14]. Additionally, the initial position of the diaphragm might change over all the requested apnea periods [14, 15]. This can lead to blurring effects and misalignment of the LV along the stack.

2. Another important characteristic of these images is the signal intensity variation: (i) over the stack due to different sensitivity along the coil; (ii) and over the slice due to cardiac flow dynamics [16] (see Fig.1.3(c)). This makes tissue classification with low-level image processing techniques, such as thresholding, a non-trivial task.

3. Normally, the number of slices acquired exceeds the size of the LV. Physicians are trained to draw contours while at least 50% of the blood-pool is surrounded by myocardium in both ED and ES [17]. The apical slice is defined as the final slice showing intracavity blood-pool at both ED and

ES (see Fig.1.3(d)). *Papillary muscles* (PM) are to be included in the volume calculations (see Fig.1.3(c)). This makes manual delineation prone to inter- and intra-observer variability, which is highly dependant on the physician experience [17].

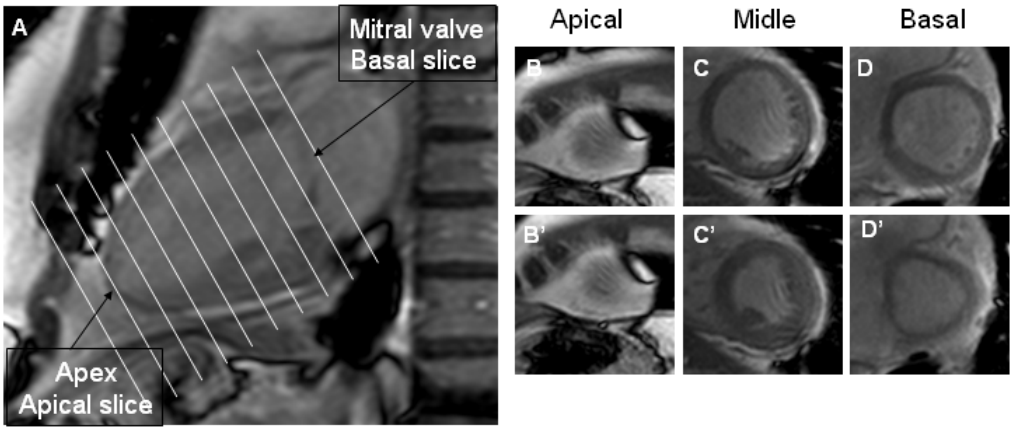

Figure 1.3: SA cine-MR images. (a) Long axis view and planing of the SA images (b) Appical slice (c) Middle slice (d) Basal slice. Top row is at ED phase and inferior row at ES phase.

Due to the stated reasons, there is a growing demand for objective, reproducible and automated technique for quantification of the LV function. However, it is also clear that a full automatic and 100% successful segmentation method is difficult to achieve. The physician will allways be essential to supervise the outcome and adjust the result if needed.

1.3 LV segmentation algorithms

According to Pham, Xu and Prince review [18], there are eight segmentation categories: (i) thresholding, (ii) region growing, (iii) classifiers, (iv) clustering, (v) *Markov random fields* (MRF), (vi) neural networks, (vii) deformable models, and (viii) atlas-guided. The first five approaches are considered pixel-classification methods and the last three are model-based methods.

In what concerns LV segmentation in SA cine-MR images, simple pixel-classification methods can only be used as initial steps in a sequence of image processing operations [18, 19, 20]. They do not take into account the spacial characteristics of an image nor they are robust enough to overcome the complex signal variation over these images. Fuzzy theory can be introduced to improve pixel-classification approaches [21, 16].

In model-based methods, the contour extraction algorithm is normally based in energy minimization between image information and *à priori* information such as the LV shape. Therefore, geometric information is incorporated along with tissue signal characteristics.

Deformable models (DM) are physically motivated techniques for delineating region boundaries by using parametric curves or surfaces that deform under the influence of internal (geometric information) and external forces (data information) [22]. Several related works can be found in the literature: based on active contours (also known as *snakes*) (2D) [23, 24, 25, 26] or deformable surfaces (3D) [27, 28, 29, 19].

In the past few years, there have been significant efforts to improve the use of DM, either in the development of the external forces or on the use of *à priori* knowledge in the internal forces.

The external forces are tunned with pre-processing tools. They can be used to smooth the image, clear artifacts and highlight the transition between the blood-pool and the myocardium. To perform this last task an edge-detector such as Canny's [30] can be used in the simplest approach. As it was previously stated, low-level pixel-classification methods can also be used, along with morphological operators.

In what concerns to the internal forces, several researchers cast the DM fitting process in a probabilistic framework and include prior knowledge of object shape by incorporating prior probability distributions on the shape variables to be estimated [27, 28, 31, 32, 33, 34]. For instance, MRF modeling itself is not a segmentation method but a statistical model that can be used within segmentation methods [35]. Two-component model analysis are also used [36], as well as the Bayesian framework [37], although they are not referred in [18].

All these combined approaches significantly decrease the amount of user interaction that is needed for estimating the LV volume. Moreover, automating the initialization procedure of such methods would also eliminate inter- and intra-observer variability from the analysis, increasing its reproducibility.

There are several levels for human intervention in the semi-automatic algorithms. One can just be selecting a *bounding box* (BB) or identify a region, such as in [20, 38] to locate the LV or the blood-pool in the image. A manual initialization of the snake can be requested due to the initialization difficulties in active contours. The snake can be initialized either by selecting a central point for a circumference [27] or manually inserting the initial snake points [37].

Although the previous approaches may prove to be robust for semi-automated LV functional analysis, to achieve a completely automated LV segmentation method that requires little or no user interaction, one must also have a robust method for automated LV cavity location in the image volume. The related works that intend to solve the LV location problem rely on cardiac SA cine-MR specific characteristics. They usually follow two approaches to locate the LV: (i) take into account the signal change over time due to muscle contraction [39] or (ii) use the *Hough Transform* (HT) based on the prior knowledge about the circular shape of the transversal cross sections of the LV [40]. Other approaches use multiple views to automatically identify the LV, such as the one proposed in [16].

In these cases, the observer might have to adjust intuitive parameters from thresholding or from morphological operators [39].

1.4 Motivation

To summarise, the LV function analysis is currently performed manually in the clinical routine in a labor, time-consuming, operator biased task. Since the nineties, the computer vision knowledge has been introduced in medical image analysis as it can be confirmed in the review works from Pham *et al.* [18] and from McInerney *et al.* [19]. Since then, several developments have been made and new theories have been incorporated to improve the models.

However, in most of the proposed algorithms only a part of the stated difficulties are addressed.

Normally, the alignment problem is hardly addressed and few give robust solutions concerning the signal variation over the slice and over the different image planes. Attending to these considerations, no fully automatic initialization is achieved using a single view of the LV.

According to this lack, a new approach must be used, combining most of the proposed models and methodologies and attending to all the SA cine-MR difficulties in order to achieve an improved, robust and fully automated LV segmentation.

1.5 Goals and original contributions

In this thesis, the first steps toward a fully automatic LV segmentation algorithm based on a single view are presented:

1. **Automatic crop**: selects a sub-volume containing the LV in all images and in all temporal frames from the acquired data. The algorithm here proposed incorporates two basic knowledges: (i) the LV shape is circular and (ii) there is a high temporal variability of the image intensity in the myocardium boundaries. Another important assumption is adopted and validated: although the heart location may vary from exam to exam, the LV will never be found at the edges of the FOV and it is always close to the center of the image. A paper on this issue was already submitted (see chapter 7).

2. **Alignment-by-reconstruction**: novel technique to solve the misalignment due to respiratory motion, inspired on the work from Sanches *et. al* [1] in ultrasound. First, the images are blurred and a translation vector is estimated using cross-correlation between consecutive slices. Secondly, a volume reconstruction is performed, where the information in a given slice is difused over its neighbors. Therefore, in the third step, the translation vector from the cross-correlation between the slices from the reconstructed volume and the original stack considers the energy from the neighbor slices.

3. **Segmentation**: The LV is segmented using active contours in an energy minimization formulation with GVF as external field. The automatic initialization algorithm here implemented is original, and it is based on the property of intersecting chords.

Tests using synthetic and real data have proven the robustness of theses algorithms and its utility in the clinical practice. Due to time limitations, it was not possible to quantify the accuracy from some steps of the algorithm. However, the results were visually inspected by an expert.

1.6 Overview

This thesis is organized in 7 chapters, where the Introduction is the first one and the Conclusion and future work is the last one. In chapter 2 there is the problem formulation along with the work-flow of the solution. From chapter 3 to 5 the three steps shortly described above are explored. In chapter 6 the Results are presented and discussed.

Chapter 2

Materials and method

2.1 Problem formulation and algorithm structure

The segmentation of the LV from cine-MR images is not a trivial issue. The signal variation across the slice and over the volume and the misalignment are some problems that must be addressed before starting the segmentation. The figure bellow presents the work flow of the proposed solution.

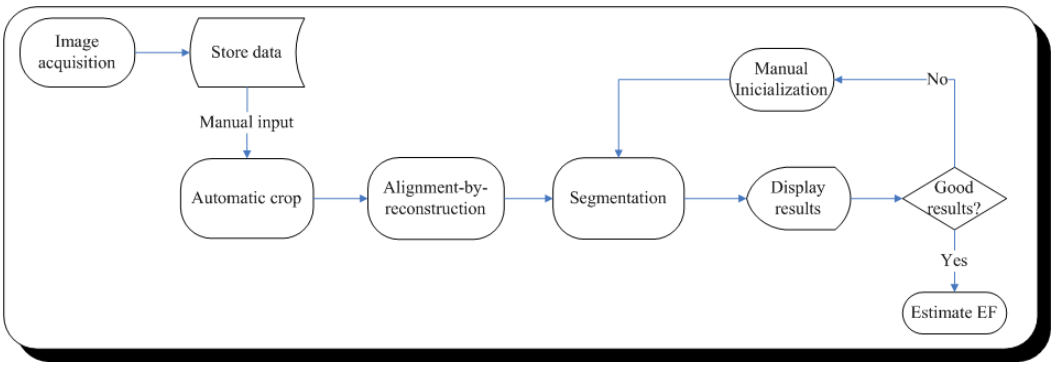

Figure 2.1: Algorithm setup

The solution here presented can be described as hybrid *bottom-up* and *top-down*. The *bottom-up* processing steps are used to bring the information to a level higher than pixel level, such as filtering and edging. These techniques are used in the first two steps, along with higher level processing techniques (HT and cross-correlation, for instance). Then *top-down* processing steps are also used, in the third step, with shape based representation to fit the data in the segmentation algorithm.

The sequence order of the algorithms is determined by efficiency. The cropping task must be performed firstly to decrease the computational burden of the alignment and segmentation tasks. The joint image registration and volume reconstruction is performed secondly in order to be able to use the initialization of the snake in one slice on the consecutive ones.

The algorithm was implemented in Matlab R2007b and the cross-correlation, reconstruction, GVF and snake initialization algorithms were implemented in c frame and compiled using *mex*. In typical conditions it spent about 2 minutes for the all processing and loading the final cropped volume, normally

less then 1 minute to compute the alignment (up to 3 minutes when the number of slices increases) and less then 10 seconds to estimate the snake initialization. Once the tunning of the segmentation parameters is correct, the segmentation algorithm spent about 20 seconds.

2.2 MRI data

The presented algorithm was tested on 17 cardiac patients identified with the letters from A to Q (five females and twelve males, mean age 48 years old, ranging from 19 to 86) from *Sociedade Portuguesa de Ressonância Magnética* (SPRM) where the LV function was studied. Prof. Ana G. Almeida was the physitian in charge, who also validated the obtained results.

The images were acquired on a 3T Philips scanner, using a Philips SENSE cardiac coil six-elements and saved in DICOM (*Digital Imaging and Communications in Medicine*). The cine-MR study was gated to the ECG and acquired with steady state free precession image sequence. A series of 8 up to 14 SA slices encompassing all the LV length were acquired over 20 up to 30 time frames over the cardiac cycle. The slice thickness is of 7 mm with a 3 mm gap between them. The spacial resolution varies between 0.71pixel/mm to 1.44pixel/mm. The *field of view* (FOV) varies between 256×256 to 672×672. The *repetition time* (TR), the *echo time* (TE) and the *flip angle* (FA) TR/TE/FA varies $4.0 - 4.7/2.0 - 2.6/15^\circ - 60^\circ$. Most of the images were acquired the following set of values: spacial resolution of 1.38pixel/mm, FOV of 560×560 and TR/TE/FA of $4.1/2.0/45^\circ$. For more details see section 7, Table 7.1.

Notation

Over the report, the notations used to access the 3-D+T data-set is listed in the table bellow:

Table 2.1: 3-D+T notation

Notation	Description
(i, j)	Pixel coordinates in the image, where $1 < i, j < M, N$
$[M, N]$	Image size
(i, j, s, t)	Voxel coordinates, where $1 < i, j, s, t < M, N, S, T$
s	Slice index, where $s < S$ being S the total number of slices
t	Time frame index, where $t < T$ being T the total number of time frames
$[M, N, S, T]$	Data-set dimensions

Let the position in a 2-D image be defined as (i, j) were $1 < i, j < M, N$, with $[M, N]$ being the size of the image; the slice index is defined as s, where $s < S$ being S the total number of slices in the data set; and the time frame index is defined as t, where $t < T$ being T the total number of time frames in the data set.

Chapter 3

Automatic Crop

As previously stated, LV function is assessed by using SA cine-MR images that represent large amounts of data: 10 up to 17 volume images over 15 up to 30 frames in the cardiac cycle.

The state of the art algorithms for LV segmentation are semi-automatic allowing to reduce significantly the human intervention. A fully automatic approach requires time consuming signal pre-processing tasks to compensate, in one hand, for coil sensitivity that induces intensity fluctuations across the images and, in the other hand, for misalignments due small movements during the breath-hold acquisition protocol. Therefore, a reduction of the matrix dimension is needed to reduce the computational burden associated with the pre-processing. alignment and segmentation algorithms. Additionally, the total amount of available data is usually large, *i.e.*, the SA cine-MR images typically have 560×560 pixels covering a FOV containing the heart and much more. Therefore, the development of an automatic crop function suits for a first step in the LV segmentation.

3.1 State of the art

To calculate the *region of interest* (ROI) it is necessary to locate the LV. One of the most simple and successful methods is described in [39]. It is based in the high temporal variability of the image intensity in the myocardium boundaries. The main drawback of this algorithm is to have two tunable parameters on which it depends.

Other approach proposed uses a size invariant circular HT to locate the LV and estimate a ROI [40]. They use Otsu's method followed by a morphological operator to segment a connected region where the point calculated by the HT will fall. This method does not take into account the signal change along the slice which makes the thresholding method less robust.

The algorithm here proposed incorporates both strategies: (i) the knowledge that the LV shape is circular and (ii) there is a high temporal variability of the image intensity in the myocardium boundaries. Another important assumption is adopted and validated: although the heart location may vary between exams, the LV will never be found at the edges of the FOV and it is always close to the center of the image. This is based on the well-known anatomic location of the heart. Under these assumptions, a fully

automatic crop algorithm is present to calculate a ROI containing the LV. This ROI is then extended to the entire stack of images over all the cardiac cycle frames, resulting in a 3-D+T cropped volume.

The algorithm was first implemented by estimating the center of a fixed-size predefined width ROI based on the circular HT. A refinement step was also implemented, where the center coordinates and width of the previous ROI are refined in and adaptive way.

3.2 Algorithm description

Let $x(i,j,s,t)$ be the $(i,j)^{th}$ voxel in the s^{th} slice at the t^{th} time frame, where $1 < i,j,s,t < M,N,S,T$. A *standard deviation* (STD) map is computed according to Eq.3.1, using all temporal frames from the middle slice of the SA images stack (see Fig.3.3(b)). As [39] suggested, high STD is found between the myocardium and the blood-pool. Additionally, this map will introduce extra ringing around the LV borders, i.e., more circular shapes. Therefore, the *à priori* knowledge of the circular shape is used to locate the LV in the STD map using the HT.

$$STD(i,j) = \sigma_t(i,j) = \sqrt{\frac{1}{T}\sum_t \left(x\left(i,j,\frac{S}{2},t\right) - \mu_t\left(i,j,\frac{S}{2}\right)\right)^2}, \tag{3.1}$$

where $\mu_t\left(i,j,\frac{S}{2}\right)$ is the mean of the signal over the time, estimated in the position $\left(i,j,\frac{S}{2}\right)$.

Before calculating the STD map, the images are filtered by a Gaussian mask to reduce the noise. This reduction is important to guarantee that the STD map observed is mainly generated by temporal variations and not by spatial noise.

The Canny edge-detector [30] is used over the STD map to get an edge-map to be used in the circular HT algorithm (see Fig.3.3(c)).

The HT originally implemented by Hough [41] was used to detect simple shapes like straight lines described in a parametric form. In the circular HT here used [42], the circumference is defined by its center (a,b) and its radius r. Therefore, a 3D Hough parametric space is used. If the circles in an image are of known radius r, then the search can be reduced to 2D. The objective is to find the (a,b) coordinates of the centers. The true center point will be common to all parameter circles, and can be found with a Hough accumulation array (Fig.3.1). The circular HT algorithm here implemented[1] is computed for a fixed radius and the output is an accumulator **Acc** with the same dimensions of the input image $[M,N]$. The value at $Acc_r(i,j)$ represents the number of circles with radius r centered at the edge pixels that intersect the $(i,j)^{th}$ pixel.

Based on the knowledge that the LV centroid is the center of multiple circles (the ring generated in the STD map and of the epicardial and endocardial border) and that the LV has variable size, the HT is computed for a set of different radius values. The maximum radius of the LV (at the end of the diastole) can range from 18mm to 28mm [43] in normal hearts. Using this interval as reference, the HT was calculated for radius ranging from 15mm to 40mm . The maximum radius was increased to 40mm

[1] "Circle detection via standard Hough Transform" from Amin Sarafraz, downloaded from Matlab Central http://www.mathworks.com/matlabcentral/fileexchange/

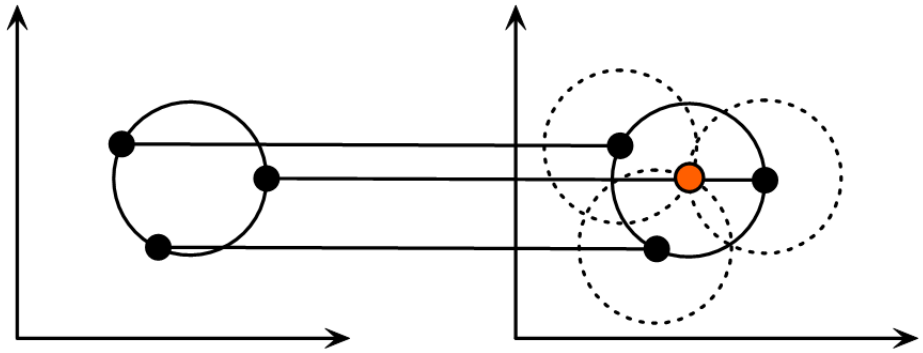

Figure 3.1: Circular Hough transform: Each point in geometric space (left) generates a circle in parameter space (right). The circles in parameter space intersect at the center of the original circumference in the geometric space

in order to include the epicardial border of the LV, and the minimum was decreased to 15mm because the middle slice of the stack might not correspond to the largest section of the LV. With steps of 2mm of interval, the circular HT is processed for all the radius from 15mm to 40mm and the accumulators are added at each step (Eq.3.2). The $\mathbf{Acc}_{Total}$ incorporates the whole information about circles with every radius in the range, amplifying its common center location. Adding the accumulators will ensure that the maximum will be closer to the centroid of the LV.

$$Acc_{Total}(i,j) = \sum_{r} Acc_r(i,j) \tag{3.2}$$

Based on the assumption that the LV is always close to the center of the image, the circles detected close to it will be favored. The $\mathbf{Acc}_{Total}$ is then multiplied by a mask that has unitary value in a circular region around the center of the image and with decreasing values up to the borders, following Eq.3.3 and showed in Fig.3.2.

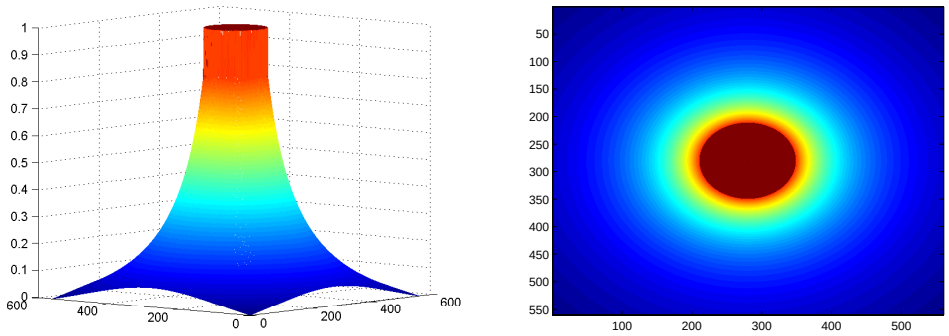

(a) 3D view

(b) top view

Figure 3.2: Accumulator mask used to reduce the importance of the detected circles outside the central circular region.

$$h(\mathbf{x}) = \begin{cases} 1 & \text{if } \|\mathbf{x}-\mathbf{c}\| \leq R \\ \left(\frac{1}{\|\mathbf{x}-\mathbf{c}\|} - \frac{1}{\|\mathbf{c}\|}\right) \cdot R & \text{if } \|\mathbf{x}-\mathbf{c}\| > R \end{cases}. \tag{3.3}$$

where $\mathbf{c} \in R^2$ represents the center of the image, $\mathbf{x} \in R^2$ the position of a mask element and $R = 50$mm, related with human anatomy. This value is fixed and was selected based on experimental tests and on the results from [16]. This reference radius determines the maximum possible distance from which the LV centroid is apart from the center of the image and the circular region where the $\mathbf{Acc}_{Total}$ has unitary weight. Outside this region the $\mathbf{Acc}_{Total}$ is weighted by smaller values, reducing the importance of the detected circles in this area. The mask is zero at the corners of the image. The new ROI is squared and centered at the coordinates of the maximum of the $\mathbf{Acc}_{Total}$. The side dimensions of this BB were set to $(2 + \epsilon)r_{max} = 120$ mm, where $\epsilon = 1$ is a safety coefficient and $r_{max} = 40$ mm.

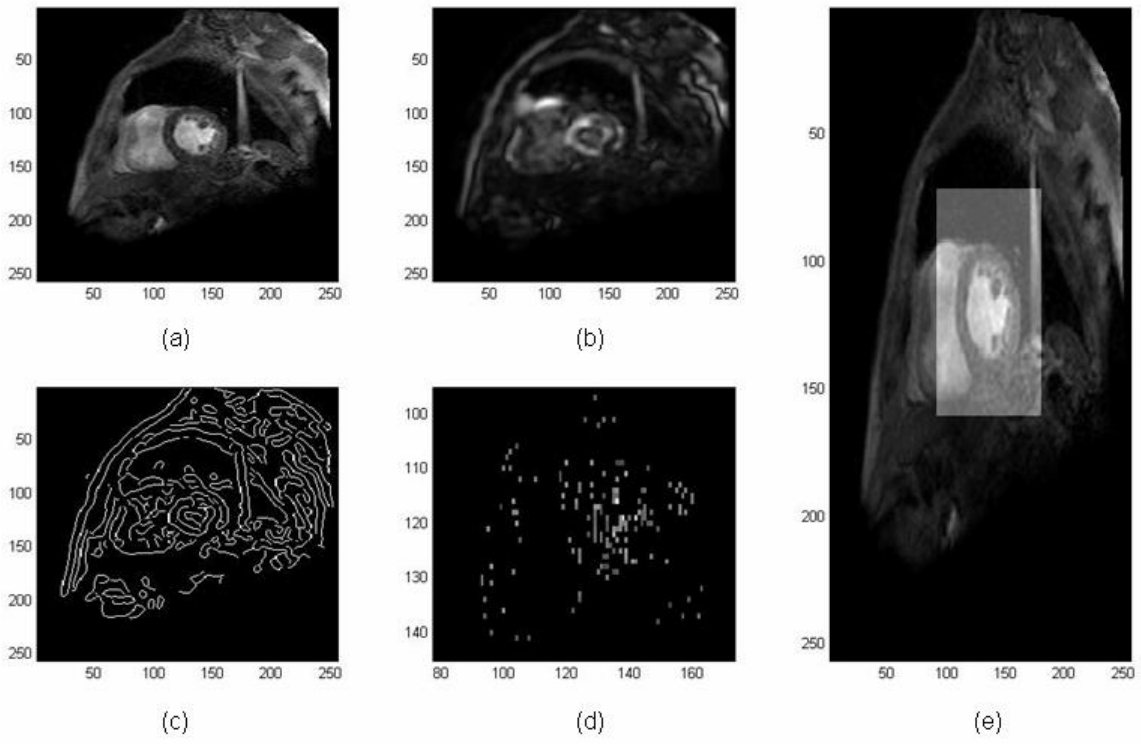

Figure 3.3: Automatic crop results from patient Q. (a) original image (middle slice 2^{nd} time-frame) (b) STD map (c) Canny edge-map (d) Filtered accumulator map, zoomed into the area where the accumulator has higher intensity (e) Resulting BB highlighted in the original image.

Adaptive LV windowing

In the first step of the algorithm, a fixed size window is generated, only depending on the pixel resolution. All the tested data-set had successful results, *i.e.*, the myocardium was always within the window (see Fig.3.3 as an example). However, it is not able to consistently locate the exact center of the LV, and for that reason, the estimated ROI is not the smallest possible.

The goal of this refinement step is to improve the center and radius estimation and adjust the window. The HT is again used for a set for radius, however the accumulatores will not be added up: the most voted center will be selected for each radius. Additionally, a growing BB will be used, in order to eliminate the influence of bigger structures in the smaller boxes, highlighting the optimal radius peak. The box size increases from $2r_{min} = 30$mm to $3r_{max} = 120$mm, with 10mm gap between iterations. Let $D(k)$ be the

width of the box at k^{th} step of the growing BB and $\mathbf{x} \in R^2$ a position in the accumulator matrix. The new parameters to generate an adaptive window are estimated by Eq.3.4. The range of radius used in the first step is also used here. The new squared BB is centered at $\mathbf{c}_{adaptive}$ and with width $(2+\epsilon)r_{adaptive}$, where $\epsilon = 1$ is a safety coefficient.

$$(r, \mathbf{c})^{new}_{adaptive} = \arg\max_{r,\mathbf{x}} \mathbf{Acc}_{r,D(k)}(\mathbf{x}) \tag{3.4}$$

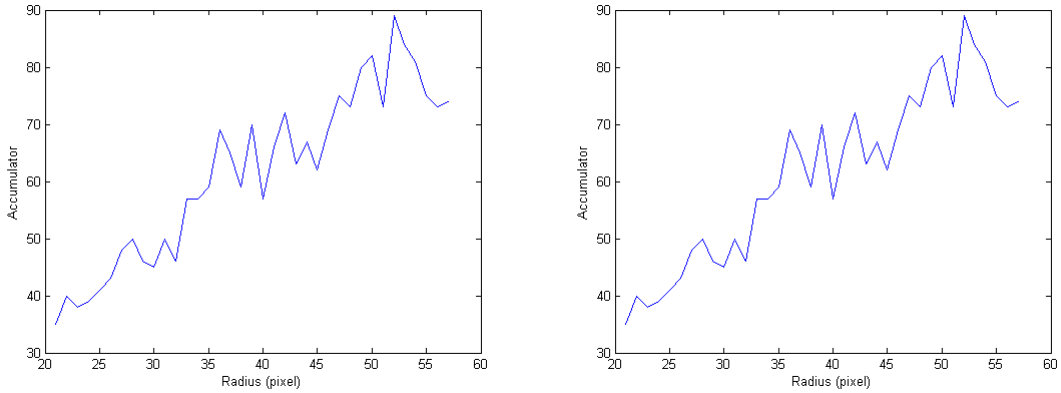

(a) Patient E

(b) Patient G

Figure 3.4: Graphics from the biggest BB, radius vs accumulator.

In Fig.3.4 it is possible to observe the resulting graphics representing the accumulator weight for each radius for the biggest BB in two different patients. There were no significant differences over the set of BB tested, therefore only the results from the biggest one are presented. The graphics clearly have an offset that increases with the radius. That is expected since the perimeter increases with the radius, therefore the weight in the accumulator increases as well. This effect was compensated by dividing the accumulator value with the radius to eliminate the influence of the size (not shown). It would be expected to have a peak at the optimum radius. However, that is not the rule, and most of the times the peak is in the higher radius, due to the offset and the implemented compensation was not able to overcome this difficulty in a consistent way.

Observing the results, the peak criterion itself was not always good: 4 out of the 17 studied cases had bad fitting (Fig.3.5), *i.e.*, the BB was to tight, cutting out the epicardium, and not robust to the misalignment. But these *unsuccessful* cases were actually the most successful ones, because the selected radius was the closest to the endocardium, and an increase in the constant factor would be enough to have a good fit. However, in most cases the estimated radius is higher due to the biased accumulator resulting in BB bigger then the ones from the first step. The observed results were not successful and will not be used in the further steps.

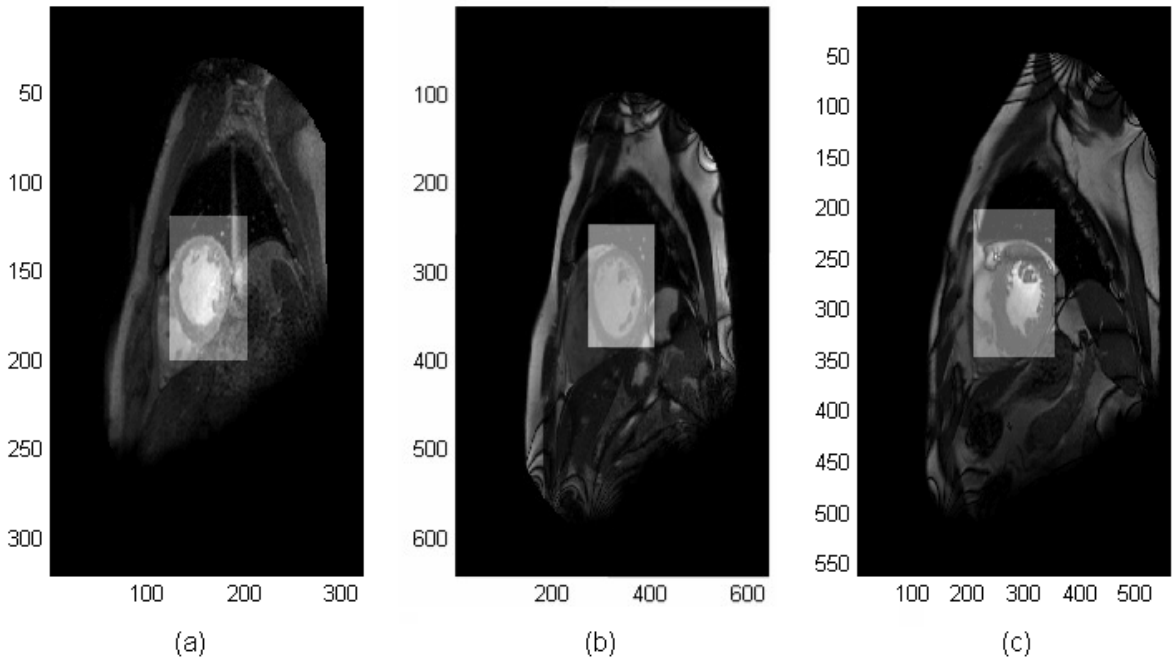

Figure 3.5: Automatic crop results with adaptive LV windowing. (a) Patient E (b) Patient K (c) Patient I.

Chapter 4

Alignment-by-reconstruction

Although many advances have been made in cardiac MRI, the heart motion during image acquisition remains a source of artifacts. The motion of the heart is generated by the cardiac cycle beating and normal respiration, admitting that the patient holds still during the entire exam.

In order to compensate for the heart beat, the acquisition is gated to the ECG. Dual cardiac-respiratory gating is more complex because the respiratory motion is generally less reproducible than the cardiac cycle. The existing gating methods tend to acquire during short periods of the respiratory cycle, typically at end-expiration, when the motion of the heart is smaller. Therefore, it is still no efficient and out of the clinical routine. For this reason, the standard acquisition protocol in LV function studies is performed in breath-hold conditions.

However, several studies showed that there is residual heart motion during breath-hold acquisitions [15, 10, 14]. During suspended respiration, there is a displacement of the diaphragm and the heart does not return to the same position on consecutive heart beats [14]. Additionally, the initial position of the diaphragm might change over all the requested apnea periods [14, 15]. This can lead to blurring effects and misalignment of the LV along the stack.

4.1 State of the art

Most of the LV registration and alignment algorithms found in the literature refer to the registration of images from different imaging modalities [44] or to build statistical models [34, 31, 45]. Alignment algorithms that solve the misalignment between consecutive planes (further referred as *intra-plane* alignment) were not found as an independent research topic in the literature, although some full automatic LV segmentation algorithms referred this problem [36, 16, 20].

In these algorithms, two different approaches were used: (i) locate the LV centroid at all the LV slices and align then according to that centerline [46] or (ii) combining multiple views, for instance, short-axis and long-axis views [36, 16]. The use of the first technique is not efficient since it cannot benefit from the initialization in one slice to initialize the segmentation in the adjacent slices.

The alignment of the cardiac planes is a non-trivial registration task. The problem is to align a set of

misaligned slices instead of registering different views of the same object (see Fig.4.1). The use of mutual information is not the most adequate method to solve this problem, because the solution with minimal energy leads to overlapping contours, while the solution relies in concentric contours. The presence of structures that not change between planes is important to the convergence of the algorithm to the desired solution (in the synthetic example in Fig.4.1(a), the small rings play that role).

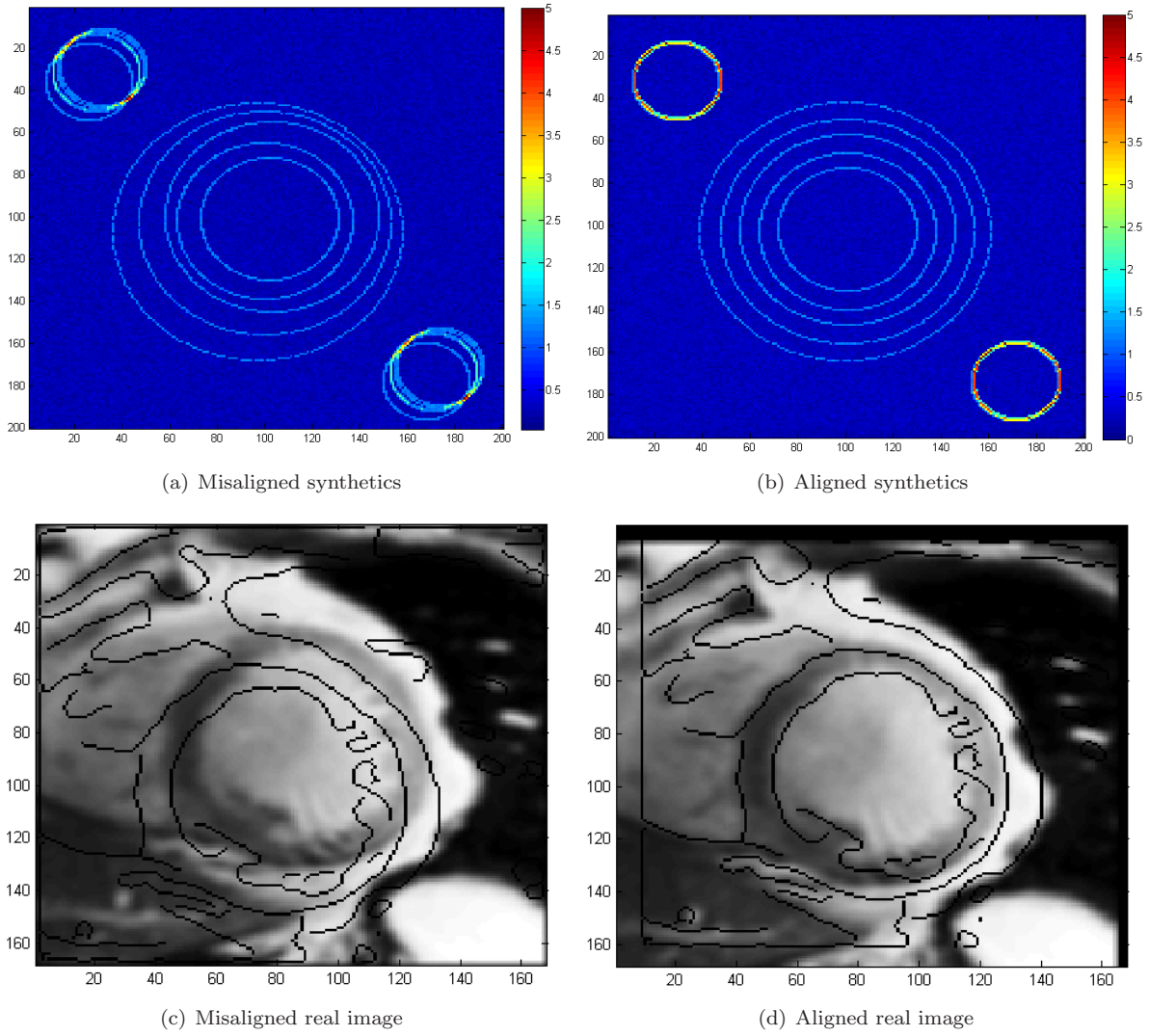

(a) Misaligned synthetics

(b) Aligned synthetics

(c) Misaligned real image

(d) Aligned real image

Figure 4.1: Misalignment in cardiac images: example with synthetics and real images

Here, a joint image registration and volume reconstruction is proposed, inspired on the previous work from Sanches *et al.* [1] in ultrasound. However, its goal was the reconstruction of the volume using an alignment step, while here the reconstruction is used the achieve an optimal alignment.

4.2 Algorithm description

Let $\mathbf{Y}_t^k$ be the edge map of the volume data set of the t^{th} time frame, at the k^{th} iteration step of the algorithm and $\mathbf{Y}(i,j,s)$ be the $(i,j)^{th}$ voxel in the s^{th} slice, where $1 < i,j,s < M,N,S$. The cropped data set is the input of the algorithm. The processing flow of the proposed method is described in Fig.4.2.

The pre-processing tasks will be described at the end of the chapter.

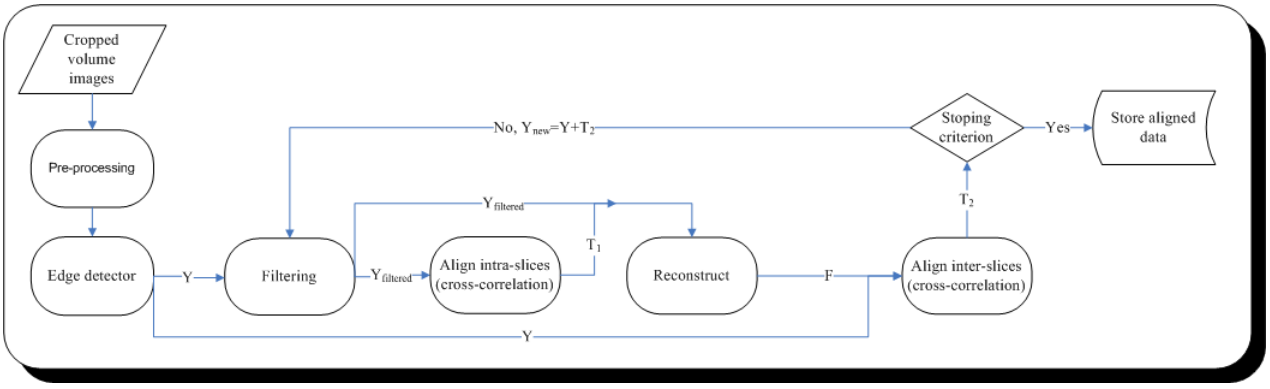

Figure 4.2: Alignment-by-reconstruction algorithm work-flow

In the first step of the algorithm, the Canny edge detector [30] is applied with a wide range in the thresholds parameter, $0.01 \rightarrow 0.1$, to get a binary edge-volume $\mathbf{Y_t}$ and guaranty that the endocardium is fully represented in the edge-map, without broken edges (Fig.4.3(a)). This binarization reduces the computational weight of the tasks that follow. Then, $\mathbf{Y_t}$ is filtered with a broad Gaussian mask (#10 and $\sigma = 5$), to diffuse the contour information.

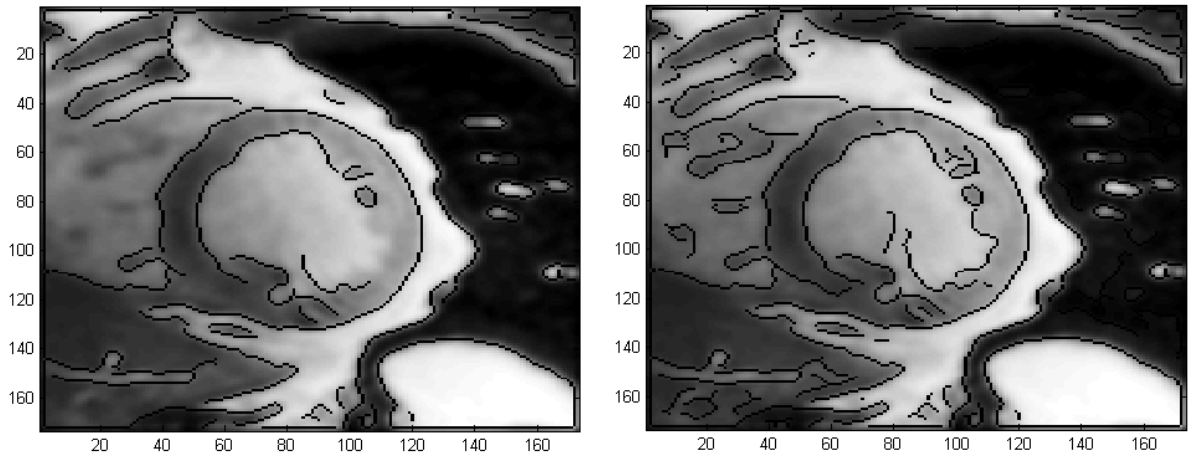

(a) Weak edges, Canny default threshold

(b) Spurious edges, Canny 0.01 - 0.1

Figure 4.3: Weak edges in cine-MR images using Canny edge-detector. The dark lines represent the edges over the original image.

In the third step, the first alignment task is performed. For the sake of simplicity, lets re-define the voxel notation $\mathbf{x}(s) = \mathbf{Y}(i, j, s)$. The translation vector $T_1^k(s)$ of the voxels $\mathbf{x}(s)$ from slice s is estimated by calculating the cross-correlation between consecutive planes of the volume (see "Intra-planes alignment" in Fig.4.4) and its average subtracted according to Eq.4.1: ,

$$\mathbf{x}^{k+1}(s) = \mathbf{x}^k(s) + T_1^k(s) - \frac{1}{S}\sum_{s}^{S} T_1^k(s). \tag{4.1}$$

This first set of planes aligned $\mathbf{Y}^0_{IntraPlanesAlignedT_1}$ is used to reconstructed the volume $\mathbf{F}^0$. This step

requires intense computation over the volume data by using cross-correlation. For this reason, cropping is essential.

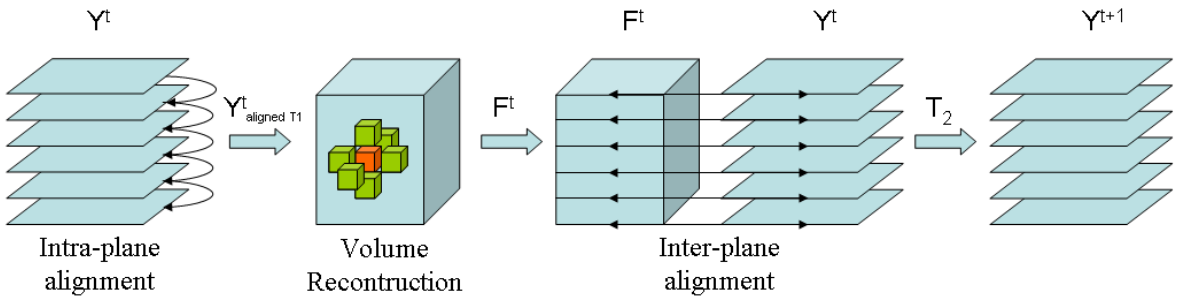

Figure 4.4: Iteration step from the algorithm

The reconstruction is the fourth step and it is an iterative process where the following energy function is minimized:

$$\mathbf{E} = \sum_{i,j,s}^{M,N,S} \left(\mathbf{F}_{i,j,s} - \mathbf{Y}_{i,j,s}\right)^2 + \alpha \sum_{i,j,s,\delta}^{M,N,S,N_b} \left(\mathbf{F}_{i,j,s} - \mathbf{F}_{i,j,s,\delta}\right)^2, \tag{4.2}$$

where N_b is the number of neighbors of each voxel and $\mathbf{F}$ is the unknown volume computed from the original data $\mathbf{Y}$ and influenced by its volume neighbors δ with and weighting factor α. To compute the minimizer of $\mathbf{E}$, $\mathbf{F}$, Eq.4.2 must be derived and equal to zero:

$$\frac{\partial \mathbf{E}}{\partial \mathbf{F}_{i,j,s}} = \left(\mathbf{F}_{i,j,s} - \mathbf{Y}_{i,j,s}\right) + \alpha N_b \left(\mathbf{F}_{i,j,s} - \bar{\mathbf{F}}_{i,j,s}\right) = 0, \tag{4.3a}$$

$$\text{where } \bar{\mathbf{F}}_{i,j,s} = \frac{1}{N_b} \sum_{\delta}^{N_b} \mathbf{F}_{i,j,s}.$$

To find the solution for this energy minimization, the Newton-Raphson method is used, leading to the following iterative equation formulation: let $\mathbf{F}_l^k$ be the l^{th} iteration step to estimate $\mathbf{F}^k$,

$$\mathbf{F}_{l+1}^k(i,j,s) = (1-K)\mathbf{Y}^k(i,j,s) + K\bar{\mathbf{F}}_l^k(i,j,s), \tag{4.4}$$

$$\text{where } K = \frac{\alpha N_b}{1+\alpha N_b}.$$

The iterative process associated with Eq.4.4 is initialized with $\mathbf{F}^0 = \mathbf{Y}$, $\alpha = 0.9$ and $N_b = 6$, six-connected. The stop criterion is:

$$\frac{\left\|\mathbf{F}_{l+1}^k - \mathbf{F}_l^k\right\|}{\left\|\mathbf{F}_{l+1}^k\right\|} < 0.1 \tag{4.5}$$

This reconstruction step is essential to diffuse the misaligned slices into its neighbors and by this influencing the next alignment step: the "Inter-planes alignment" in Fig.4.4. The translation vectors are estimated and its average subtracted according to Eq.4.1 using T_2. This iterative process stops when the

translation vector reaches the equilibrium:

$$\frac{\Delta^k}{\Delta^{k-1}} < 0.1, \qquad \text{where } \Delta^k = \left\| \sum_s^S \left| \bar{T}_2^k(s) - \bar{T}_2^{k-1}(s) \right| \right\| \tag{4.6}$$

Pre-processing

Before entering the registration/reconstruction part of the algorithm, the cropped 3-D+T data-set is first processed with low-level signal processing tools. First the data-set is normalized according to Eq.4.7. Given a gray-level image $\mathbf{I}(x, y)$, $(x, y) \in R^2$, viewed as a function of continuous positions variables:

$$\mathbf{I}_N(x, y) = \frac{\mathbf{I}(x, y) - \min(\mathbf{I})}{\max(\mathbf{I}) - \min(\mathbf{I})} \tag{4.7}$$

Then, the histogram equalizer algorithm from Matlab is used. Without specifying the desired histogram, the function creates a flat histogram and choses the gray scale transformation T to minimize Eq.4.8:

$$|c_1(T(k)) - c_0(k)|, \tag{4.8}$$

where c_0 is the cumulative histogram of $\mathbf{I}$ and c_1 is the cumulative sum of the histogram for all intensities k. This minimization is subject to the constraints that T must be monotonic and $c_1(T(a))$ cannot overshoot $c_0(a)$ by more than half the distance between the histogram counts at a. The function uses this transformation to map the gray levels in $\mathbf{I}$ to their new values.

The data-set is then filtered with a low-pass Gaussian mask (#5 and $\sigma = 2$) to reduce noisy structures. The power-law transformation (Eq.4.9) is then applied, inspired on [20]:

$$\mathbf{I}' = \kappa \mathbf{I}^\gamma, \tag{4.9}$$

where $\kappa = 10$ (because the image was normalized) and $\alpha = 1.3$ to enhance contrast.

Additionally, the 2D median filter was also used, in order to eliminate structures such as the PM and preserve the contours.

Chapter 5

Segmentation

Although originally developed for application in computer vision and computer graphics, the potential of DM in *medical image analysis* (MIA) was quickly realized. Its application in the study of LV function is now an active field of research. Manual segmentation of the LV is extremely labor intensive, time-consuming, biased, non-reproducible and experience-dependent task.

Among the first uses of DM in LV segmentation was the application of the active contours, also known as *snakes* [22]. Typically users initialized the *snake* manually near the object of interest. Once the user is satisfied with the result on an initial image slice, the segmented contour may be used as the initial boundary approximation for neighbor slices. Active contours have been developing since and are a major tool in what concerns to MIA [19], and LV segmentation in particular [33].

5.1 Background

Image segmentation, which aims at separate the image into regions, is an important step toward image analysis and interpretation [47]. Low-level segmentation techniques, such as pixel-based (thresholding), edge-based or region-based, divide the image into regions that hopefully correspond to objects. Higher-level techniques, such as DM, include knowledge about the object.

Segmentation using DM

DM are curves or surfaces defined within an image domain that can move under the influence of internal forces, which are defined within the curve or surface itself, and external forces, which are computed from the image data [48]. In this work, the 2-D DM curves are used.

DM can be described by parametric or geometric models [48]. Parametric models represent the curve in its parametric form, allowing direct interaction with the model. Geometric models represent the curve implicitly as a *level set* of a higher-dimensional scalar function. Their great advantage is the natural handling of topological changes.

In what concerns to LV segmentation, it is not expected to handle with topological changes. For this reason, the problem is going to be formulated in terms of the parametric model.

Parametric DM and energy minimization formulation

There are two types of formulations for parametric DM: an energy minimization formulation and a dynamic force formulation. Here, the energy minimization formulation [23, 33] is adopted.

Energy minimization formulation aims to find the parameterized curve that minimizes the weighted sum of *internal energy* and *potential energy*. The parametric active contour is a dynamic curve $\mathbf{C}(s) = (\mathbf{x}(s), \mathbf{y}(s))$, $s \in [0, 1]$, which moves through the spatial domain of an image in order to minimize the following energy functional:

$$\mathbf{E}(\mathbf{C}) = \int_0^1 \alpha(s) \left| \frac{\partial \mathbf{C}}{\partial s} \right|^2 + \beta(s) \left| \frac{\partial^2 \mathbf{C}}{\partial s^2} \right|^2 ds + \int_0^1 \mathbf{P}(\mathbf{C}) ds. \tag{5.1}$$

The first integral corresponds to the internal energy, the regularization term. It describes the tension and the smoothness of the contour. The first-order derivative are elastic forces. They discourage stretching and make the model behave like an elastic string. The second-order derivative models the bending forces and makes the model behave like a rigid rod. The weighting parameters $\alpha(s)$ and $\beta(s)$ are used to control the model's tension and rigidity, respectively. They are normally constant.

The second integral corresponds to the potential energy. The potential energy function $\mathbf{P}$ is derived from the image and takes smaller values at object boundaries. Typically, the potential function is based on the gradient of the image: given a gray-level image $\mathbf{I} : R^2 \to R$, viewed as a function of continuous positions variables, a typical potential energy function designed in such a way that intensity transitions become associated to valleys of the potential is

$$\mathbf{P}(x, y) = -w_e \left| \nabla [\mathbf{G}_\sigma(x, y) * \mathbf{I}(x, y)] \right|^2, \tag{5.2}$$

where w_e is a positive weighting factor, $\mathbf{G}_\sigma(x, y)$ is a 2-D Gaussian function with standard deviation σ, ∇ is the gradient operator and $*$ is the 2-D convolution operator.

The problem of finding a curve $\mathbf{C}(s)$ that minimizes the energy functional E (Eq.5.1) is known as a variational problem. The curve that minimizes $\mathbf{E}$ must satisfy the following Euler-Lagrange equation:

$$\frac{\partial}{\partial s} \left(\alpha \frac{\partial \mathbf{C}}{\partial s} \right) - \frac{\partial^2}{\partial s^2} \left(\beta \frac{\partial^2 \mathbf{C}}{\partial s^2} \right) - \nabla \mathbf{P}(\mathbf{C}) = 0, \tag{5.3}$$

which may be interpreted as the following force balance equation:

$$\mathbf{F}_{int}(\mathbf{C}) + \mathbf{F}_{pot}(\mathbf{C}) = 0. \tag{5.4}$$

To find the object boundary, parametric curves are initialized within the image domain (manually or automatically), and are forced to move toward the potential energy minima under the influence of both these forces. To find the solution to Eq.5.3, the active contour is made dynamic by treating $\mathbf{C}(s)$ as a function of time $t \to \mathbf{C}(s, t)$. The time zero contour, $\mathbf{C}(s, 0)$, is given by the initialization contour. Then,

the snake evolves iteratively according to Eq. 5.5:

$$\frac{\partial \mathbf{C}}{\partial t} = \mathbf{F}_{int}(\mathbf{C}) + \mathbf{F}_{pot}(\mathbf{C}). \tag{5.5}$$

The main advantages of the snakes are their ability to generate a parametric smooth curve from the image. However, most of the these models are sensitive to noise due to their purely edge-based nature and low attraction range of the gradient. Therefore the initialization has to be done close to the true contour. Additionally, the traditional snake model does not converge properly into boundary concavities.

Increasing σ from $\mathbf{P}$ can broaden the attraction range of the potential function making the minimum potential valleys less step. However, it can also cause shift in the boundary location, resulting in a less accurate result.

There are several formulations of $\mathbf{P}$ to extend the attraction range, in order to decrease the dependence on a good initialization: the multiscale Gaussian potential force by Terzopoulos, Witkin and Kass [22], the pressure force proposed by Cohen [49], the distance potential force by Cohen and Cohen [50] and *gradient vector flow* (GVF) presented by Xu and Prince [23] that is used in this work.

The GVF is a very attractive external force for active contour models because it addresses both problems listed above. The GVF is computed as a diffusion of the gradient vectors of a gray-level image or binary edge map derived from the image.

5.2 Gradient Vector Flow

Let $f : R^2 \rightarrow R$ be the edge map derived from the image $\mathbf{I}$ and $\mathbf{F}_{pot}(x, y) = \mathbf{v}(x, y) = [u(x, y), v(x, y)]$ where $u, v : R^2 \rightarrow R$, be the GVF field that minimizes the energy functional from Eq.5.6:

$$\epsilon = \iint \mu \left(\left|\frac{\partial u}{\partial x}\right|^2 + \left|\frac{\partial u}{\partial y}\right|^2 + \left|\frac{\partial v}{\partial x}\right|^2 + \left|\frac{\partial v}{\partial y}\right|^2 \right) + |\nabla f|^2 |\mathbf{v} - \nabla f|^2 dxdy. \tag{5.6}$$

The edge map $f(x, y)$ has three general properties: (i) the gradient of an edge map ∇f has vectors pointing toward the edges, (ii) these vectors generally have large magnitudes only in the vicinity of the edges, and (iii) in homogeneous regions, where $\mathbf{I}(x, y)$ is nearly constant, ∇f is nearly zero.

According to f properties, the variational formulation in Eq.5.6 makes the result smooth when the region is homogeneous. In particular, when $|\nabla f|$ is small, the energy is dominated by the partial derivatives of the vector field. On the other hand, when $|\nabla f|$ is large, the second term dominates the integrand and is minimized by setting $\mathbf{v} = |\nabla f|$. The parameter μ is a regularization parameter and should be set according to the amount of noise present in the image.

Euler equations are again used to solve this variational problem and calculate the GVF field:

$$\mu \nabla^2 u - \left(u - \frac{\partial f}{\partial x}\right) \left(\left|\frac{\partial f}{\partial x}\right|^2 + \left|\frac{\partial f}{\partial y}\right|^2 \right) = 0 \tag{5.7a}$$

$$\mu \nabla^2 v - \left(v - \frac{\partial f}{\partial y}\right) \left(\left|\frac{\partial f}{\partial x}\right|^2 + \left|\frac{\partial f}{\partial y}\right|^2 \right) = 0 \tag{5.7b}$$

where ∇^2 is the Laplacian operator.

LV segmentation introduces new problems where the use of active contours with GVF is not enough. Turbulent blood-flow and papillary muscles pose additional challenges on snake convergence to the object boundary. Therefore, it is important to solve this problem in both fronts. To address the first issue, a novel initialization technique was implemented. Besides statistical models or manual initialization, there are no other methods described in the literature to initialize the snake to segment the LV. In what concerns to the second issue, the median filter was used in the pre-processing step in order to eliminate/decrease the influence of the papillary structures in the blood-pool.

When non of the implemented techniques works properly, the user can always manually change the snake. Additionally, the user has to manually sellect the slices to estimate the EF, according to the protocol described in section 1.2. Due to time limitations, no solutions were found for this problem.

5.3 Automatic snake initialization

Snake initialization is a very important step in segmentation, determinant for a good convergence.

LV imaging has special characteristics that make this issue important. In one hand, edge detectors are not able to fully detect the endocardium border without detecting other spurious structures as well. These noisy structures present in the blood pool have contrast transitions close to some weak edges (compare Canny performance for different thresholds in Fig.5.1) and are generated by turbulent blood-flow.

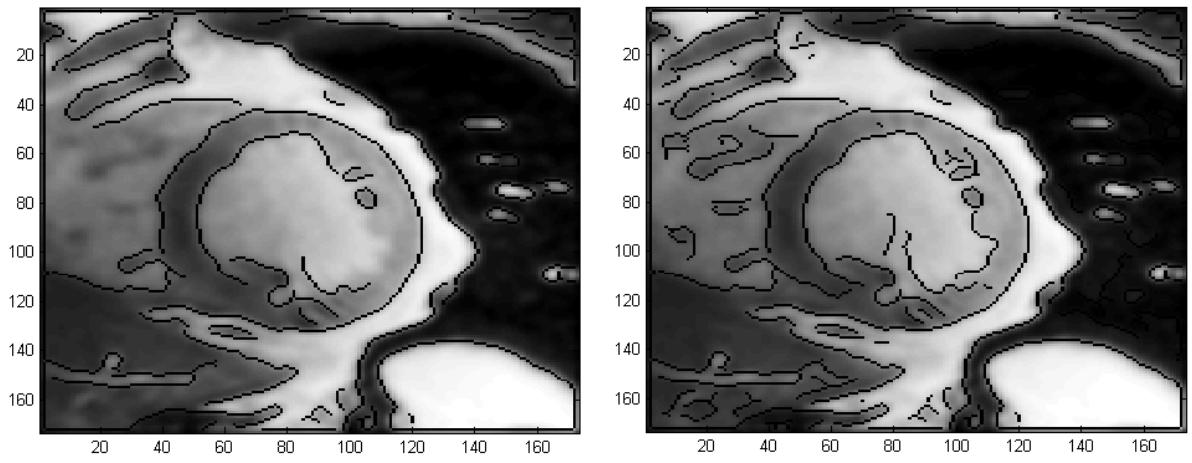

(a) Weak edges, Canny default threshold

(b) Spurious edges, Canny 0.01 - 0.1

Figure 5.1: Weak edges in cine-MR images using Canny edge-detector. The dark lines represent the edges over the original image.

On the other hand, HT does not give a satisfying center/radius estimation to initialize the contour with a circumference based on those parameters. It is a very sensitive system, and the circumference can fall out of the borders and compromise the convergence of the contour leading to a mixed epicardium-endocardium final contour or be stuck in the spurious structures such as PM.

Our approach is robust to all the difficulties in LV segmentation because is based on the gray-scale

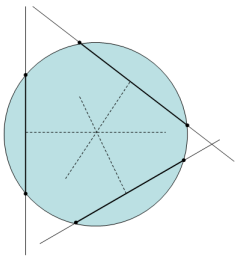

Figure 5.2: Chords

image and not on the edge-map. The only request is that the center of the image must be inside the blood-pool, which is accomplished in chapter 3. Inspired from [51], the property of intersecting chords is used. A chord is the segment of a secant line lying inside of the circumference. The perpendicular bisector of any chord passes through the center of the circumference (see Fig.5.2).

Using two chords, the center can be estimated but with no error associated. Therefore, four chords will be used to estimate more accurately the best circumference center (see Fig.5.3). The signal profiles from four direction in the image are collected: horizontal, vertical and two diagonals. It is preferable to use middle slices instead of the basal ones, where the PM are seldom, and preferably near the diastole phase [46].

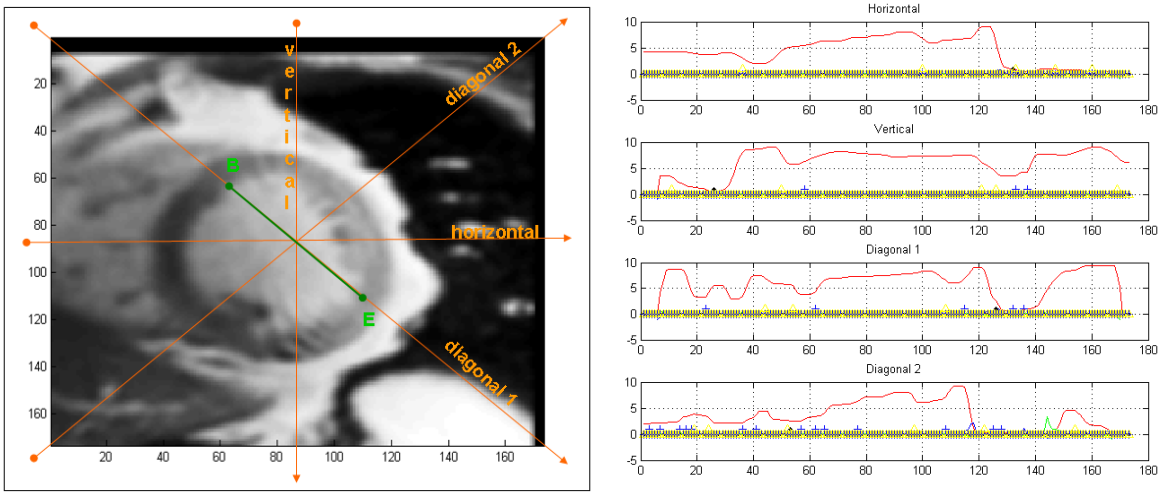

(a) Signal profile directions

(b) Signal profile

Figure 5.3: Automatic snake initialization. (*orange*) signal profile directions collected from the middle slice: the arrows point the way the signal was collected. The points 'B' and 'E' define the chord.

5.4 Implementation

The data-set from the *alignment-by reconstruction* step (the aligned and pre-processed data-set) is the input for this final step. The setup in Fig.5.4(a) explains the work-flow of this process:

The process starts at the first time frame $t = 1$ and middle slice $s = S/2$ (see Fig.5.4(b)). From this starting point, the *ES frame* (ESF) and the EDV are estimated. Based on the ECG gating, the first frame is collected at the QRS complex from the ECG, that represents the start of the systole, therefore,

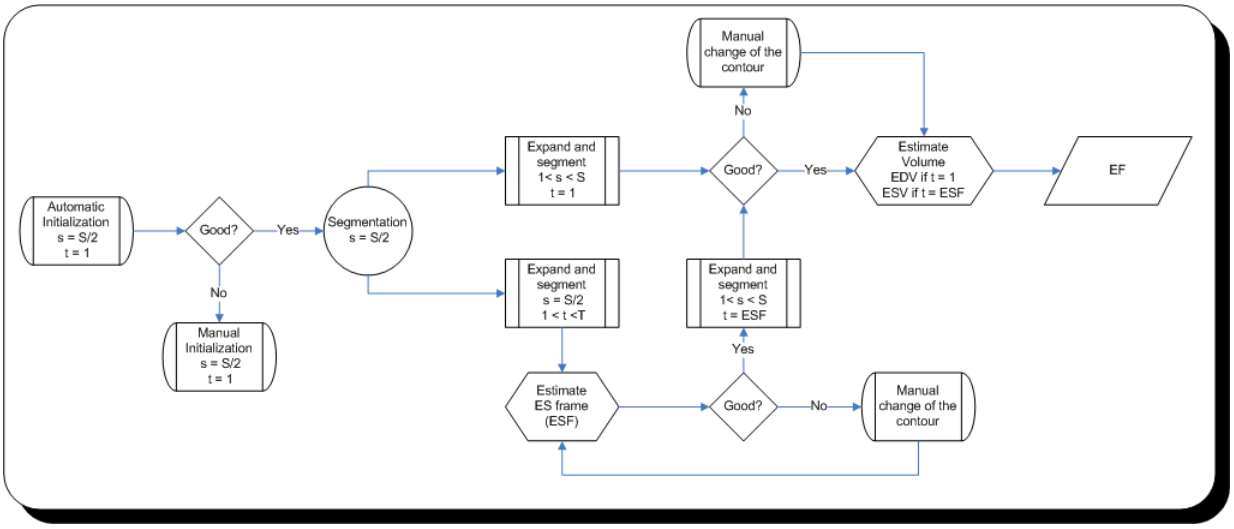

(a) Work flow

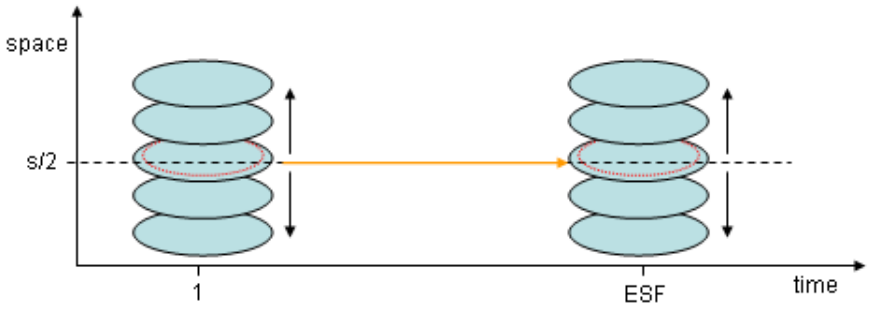

(b) Expansion of the contours in space and time domain.(*red dashed*) initialization contour in middle slice (*orange arrow*) segmentation in time domain and area measurement to estimate ESF.

Figure 5.4: Segmentation work flow

the end of the diastole. After the initialization, the segmentation algorithm is used and the contour is expanded in space and time through its neighbors, as showed in Fig.5.4(b).

Over the time domain, the area is measured and the ESF is the one with minimum area. It is expected to find the ESF at about 43% of the time course (the systole is shorter then the dyastole [52]), *i.e.*, in a set of 30 frames, it is expected to find the ESF around the 12 time frame. After estimating the ESF, the segmentation of the ESV is initialized in the middle slice and $t = ESF$ with the segmented contour from the time series. Then, the contours are again propagated over the space (Fig.5.4(b)).

After each segmentation step, the results are displayed and can be manually changed. The spurious slices that do not fulfill the criteria described in the section 1.2 have to be manually excluded.

Initialization algorithm

As previously mentioned, the initialization is based on the intersecting chords property. Four chords are used: horizontal, vertical and two diagonals. The intensity profile signals, $s(x)$, are plotted and the discrete derivative, $Ds(x)$, of each is calculated according to Eq.5.8. The point edges B are calculated in an inverse way of the E points for the sake of comparison (see Fig.5.3 to identify the points). Due to the

previously referred signal variations over the slice (Fig.5.1(a)), the estimation of B points is done with the derivative calculated forward and the E points with the derivative calculated backward in order to make the contrast value comparable.

$$Ds(x) = \begin{cases} \frac{s(x+1)-s(x)}{s(x)}, \text{ first edge B} \\ \frac{s(\mathbf{x})-s(x+1)}{s(x+1)}, \text{ second edge E} \end{cases} , x \in R \tag{5.8}$$

The local maximums of the derivative indicate for signal variations and are used to locate the endocardium border. The peaks of the derivatives with amplitude higher then 3.5% are selected and collected into arrays. The transitions higher then 60% are cutted-off by this algorithm. This mechanism is used to decrease the number of candidates resulting from the contrast between muscle and lung, higher than the normal transition between muscle and blood.

For each direction, a set of candidate chords are selected, defined by local maximums points B and E, if the pair of points (B, E) satisfies the following conditions:

- $B > E$ according to the signal acquisition direction;
- $15mm < \overline{BE} < 56mm$;
- The relative positions from each pair BE must satisfy a circumference (according to image axis in Matlab):
  - $B_x^{horizontal} < (B,E)_x^{vertical} < E_x^{horizontal}$
  - $B_y^{vertical} < (B,E)_y^{horizontal} < E_x^{vertical}$
  - $B_x^{diagonal1} < (B,E)_x^{vertical} < E_x^{diagonal1}$
  - $B_x^{diagonal2} < (B,E)_x^{vertical} < E_x^{diagonal2}$
  - $B_y^{diagonal1} < (B,E)_y^{horizontal} < E_y^{diagonal1}$
  - $B_y^{diagonal2} > (B,E)_y^{horizontal} > E_y^{diagonal2}$
  - $B_y^{diagonal2} < B_y^{diagonal1}$
  - $E_y^{diagonal1} < E_y^{diagonal2}$

From each direction there is a set of candidate points (B, E) that fulfill the presented criteria. The aim is to find the set of four chords (defined by the points (B, E)), one in each direction, where the intersection of their bisectors has minimum error (see Fig. 5.5(a)). Each candidate pair is combined with all pairs from the other directions. They are combined four at a time, one pair from each direction. The four sets of (B, E) points that satisfy these conditions will be ranked according to the distances of the intersections I_i of the bisectors from each chord to their center (see Fig.5.5 and Eq.5.9). This distance measures the error of the circle estimated by each set of four chords.

$$\bar{d} = \frac{1}{N}\sum_{i}^{N} |I_i - C|, \qquad \text{where } C = \frac{1}{N}\sum_{i}^{N} I_i. \tag{5.9}$$

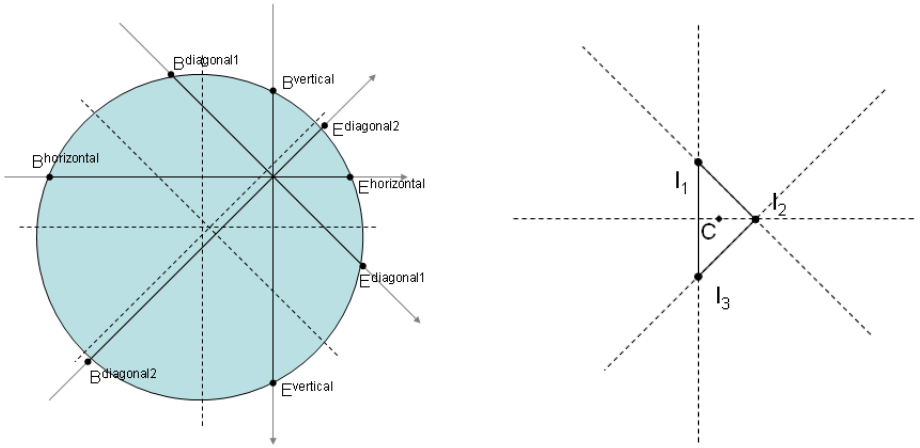

(a) Intersection of the chords (b) *Zoom in* in the intersection of the chords

Figure 5.5: Example of imperfect intersection of the chords to locate the center of the circumference. The *full lines* represent the chords and the *dashed lines* represent the bisector of the chords.

This process is repeated using the newly estimated center as the center of the new four signal profiles, in order to try to extract another set of four extra edge points. Once the set of chords is selected, they are linearly interpolated (using Matlab function). The resulting contour has sharp edges and is used as initialization for the segmentation algorithm to extract the LV contour of the middle slice of the EDV ($s = S/2$ and $t = 1$).

Numeric implementation GVF

The GVF model described in section 5.2 must be discretized for computational purposes: $\mathbf{C}(s,t) \rightarrow \mathbf{C}(i,n)$. By approximating the derivatives in Eq.5.5 with finite differences and converting the vector notation $\mathbf{C}(i,n) = \mathbf{C}_i^n = (\mathbf{x}_i^n, \mathbf{y}_i^n) = (\mathbf{x}(ih, n\Delta t), \mathbf{y}(ih, n\Delta t))$, the Eq.5.5 can be rewrote as Eq.5.11a.

$$\frac{\partial \mathbf{C}_i^n}{\partial t} = \frac{\mathbf{C}_i^n - \mathbf{C}_i^{n-1}}{\Delta t}. \tag{5.10}$$

$$\begin{aligned}
\frac{\mathbf{C}_i^n - \mathbf{C}_i^{n-1}}{\Delta t} &= \mathbf{F}_{int}(\mathbf{C}_i^{n-1}) + \mathbf{F}_{pot}(\mathbf{C}_i^{n-1}) && \text{(5.11a)}\\
&= \frac{1}{h^2}\Big[\alpha_{i+1}\big(\mathbf{C}_{i+1}^n - \mathbf{C}_i^n\big) - \alpha_i\big(\mathbf{C}_i^n - \mathbf{C}_{i-1}^n\big)\Big] \\
&\quad - \frac{1}{h^4}\Big[\beta_{i-1}\big(\mathbf{C}_{i-2}^n - 2\mathbf{C}_{i-1}^n + \mathbf{C}_i^n\big) \\
&\quad - 2\beta_i\big(\mathbf{C}_{i-1}^n - 2\mathbf{C}_i^n + \mathbf{C}_{i+1}^n\big) \\
&\quad + \beta_{i+1}\big(\mathbf{C}_i^n - 2\mathbf{C}_{i+1}^n + \mathbf{C}_{i+2}^n\big)\Big] + \mathbf{F}_{pot}(\mathbf{C}_i^{n-1}), && \text{(5.11b)}
\end{aligned}$$

where h the step size in space and Δt the step size in time. The external force F_{pot}, here the GVF field, is stored as a discrete vector field. The value of F_{pot} at any location $\mathbf{C}_i$ can be obtained by bilinear

interpolation. Setting $\Delta t = 1$, Eq. 5.11b can be written in a compact matrix form:

$$\mathbf{C}^n = (\gamma \mathbf{I} - \mathbf{A})^{-1} \left[\gamma \mathbf{C}^{n-1} + k\mathbf{F}_{pot}(\mathbf{C}_i^{n-1})\right], \tag{5.12}$$

where γ is the dammping coeficient, k is the external force weight, $\mathbf{C}^n$, $\mathbf{C}^{n-1}$ and $\mathbf{F}_{pot}(\mathbf{C}_i^{n-1})$ are $m \times 2$ and $\mathbf{A}$ is a $m \times m$ pentadiagonal matrix, where m is the number of sample points:

$$\mathbf{A} = \begin{bmatrix} a & b & c & 0 & \dots & 0 & c & b \\ b & a & b & c & \dots & 0 & 0 & c \\ c & b & a & b & \dots & 0 & 0 & 0 \\ \vdots & \vdots & \vdots & \vdots & & \vdots & \vdots & \vdots \\ c & 0 & 0 & 0 & \dots & b & a & b \\ b & c & 0 & 0 & \dots & c & b & a \end{bmatrix}, \tag{5.13}$$

where a, b, c depend on the regularization parameters α, β as follows: $a = -2\alpha - 6\beta$, $b = \alpha + 4\beta$ and $c = -\beta$.

The GVF is numerical implemented also using finite differences. Lets first define $b(x, y)$, $c^1(x, y)$ and $c^2(x, y)$:

$$b(x, y) = f_x(x, y)^2 + f_y(x, y)^2 \tag{5.14a}$$

$$c^1(x, y) = b(x, y) f_x(x, y) \tag{5.14b}$$

$$c^2(x, y) = b(x, y) f_y(x, y) \tag{5.14c}$$

To setup the iterative solution, let i, j, n correspond to x, y, t respectively, and let the spacing between the pixels be $\Delta x, \Delta y$ and the time step for each iteration Δt. Therefore, the Eq.5.7 can be re-arranged considering discretization and treating u and v as functions of time:

$$u_{i,j}^n = \big(1 - b_{i,j}\Delta t\big) u_{i,j}^{n-1} + r\big(u_{i+1,j}^{n-1} + u_{i,j+1}^{n-1} + u_{i-1,j}^{n-1} + u_{i,j-1}^{n-1} - 4u_{i,j}^{n-1}\big) + c_{i,j}^1 \Delta t \tag{5.15a}$$

$$v_{i,j}^n = \big(1 - b_{i,j}\Delta t\big) v_{i,j}^{n-1} + r\big(v_{i+1,j}^{n-1} + v_{i,j+1}^{n-1} + v_{i-1,j}^{n-1} + v_{i,j-1}^{n-1} - 4v_{i,j}^{n-1}\big) + c_{i,j}^2 \Delta t \tag{5.15b}$$

$$\text{where } r = \frac{\mu \Delta t}{\Delta x \Delta y}$$

The GVF field was computed using $\sqrt{N}$ (according to [23]). The potential field used was the one described in Eq.5.2. The Gaussian masked used, and other pre-processing tasks, were already described in section 4. The set of parameters α, β, γ, k were adjusted to each patient and for the initialization, time series and space series.

When the snake ends the deformation process, the curve is resampled to a curve with equally spaced points ($2mm$). Resampling is essential because the model used does not consider the decrease or increase of the size of the shape. Additionally, the parameters α and β are adjusted according to the curvature

evolution, when that information was available (not of the two first slices to segment):

$$\alpha_s = \alpha_{s-1}\left(1 + \mu\frac{K(s-1) - K(s-2)}{K(s-2)}\right), \tag{5.16}$$

where $K(s)$ is the curvature (estimated has $1/r$ where $r = \frac{P}{2\pi}$ as P being the perimeter of the curve) at the s^{th} slice. The parameter μ was also adjusted.

Chapter 6

Results

LV function is assessed by using SA cardiac cine-MR images that represent large amounts of data: 10 up to 17 volume images over 15 up to 30 frames in the cardiac cycle. This data is inspected manually by an expert and contours are drawn manually to extract the EF value. It is a time consuming process and its full automatization is of great interest.

The work here presented describes three automatic first steps toward a full automatization of the LV segmentation in cine-MR images: crop, registration and initialization of the segmentation. The segmentation step itself, based on active contours, still requires human intervention for a satisfying result. The algorithms here proposed were tunned and tested with images acquired from 17 patients identified with letters from A to Q. The most important results from the three steps are summarized in Table 6.2.

Automatic crop

The success of the cropping algorithm depends on whether the BB is able to fully contain the LV. The contents of the estimated BB for all the data-sets were visually inspected for every slice over all time frames. The quantification of the image size reduction is presented in the summary Table 6.2.

All the tested data-sets had successful results, *i.e.*, the LV was always within its borders. Even considering the misalignment between consecutive planes, the LV endocardial and epicardial borders were always inside the estimated fixed-size window. In Fig.6.1 it is possible to see an example of the results from patient Q. In the STD map it is clear the ringing effect resulting from alternating high and low STD areas due to muscle contraction and in the Canny edge-map it is possible to see circular structures in the LV region. In the accumulator map it is possible to identify the brighter pixel close to the LV center (around 140 in the x direction and 120 in the y direction). The last image displays the estimated ROI.

Here, the reduction only depends on the resolution of the image. In most of the cases, the size of the cropped images is equal to 30.0% of the original image. The biggest reduction was 25.4% with patient J, and the worst case was observed in patient Q, with a reduction to 34.0% of the original size (see Table 6.2).

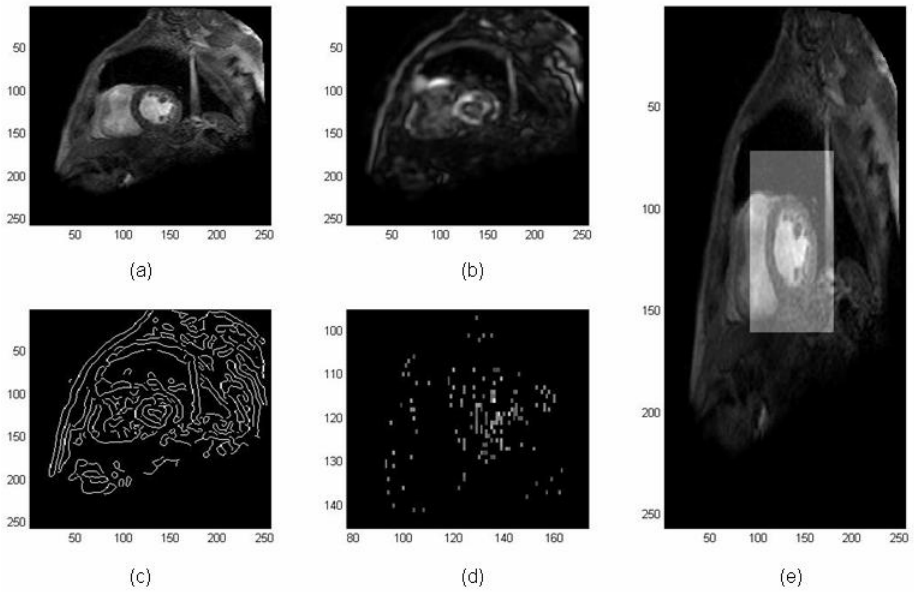

Figure 6.1: Automatic crop results from patient Q. (a) original image ($s = S/2$ and $t = 2$) (b) STD map (c) Canny edge-map (d) Filtered accumulator map, zoomed into the area where the accumulator has higher intensity (e) Resulting bounding box highlighted over the original image.

In Fig.6.2(a) and Fig.6.2(b) it is possible to observe the estimated ROI in images with resolutions different than the usual, where the algorithm performed successfully: 672×672 in patient J and 256×256 in patient Q. As previously mentioned, the signal intensity is not constant over the volume due to differences in the sensitivity along the coil and also along the slice due to cardiac flow dynamics [16]. This algorithm proved to be robust to signal variation over the image, which is usually a difficulty that must be dealt with. The proposed algorithm is able to cope with this problem because it does not depend directly on the original image but on the STD map, which decreases its sensitivity to these fluctuations.

Furthermore, cine-MRI are acquired along several breath-holds from the patient, in order to prevent respiratory motion artifacts. This can lead the misalignment of the LV along the stack [14] if the subject is not able to hold its breath properly during each volume acquisition time slot. Although the algorithm only takes the middle slice to calculate the BB, it has proven to be robust to plane misalignment, mainly because they are usually small and the cropped window is big enough to fit them.

The algorithm is not able to consistently locate the exact center of the LV because usually it is not a trivial task to define it. This is shown in the results from patient H and I in Fig.6.2(c) and Fig.6.2(d) respectively. Although the center was not located successfully, the center of the BB is close enough from the LV centroid and the whole LV is inside the BB. The algorithm locates another circular structure close to the LV, like the myocardium that encloses the LV and the right ventricle, who's center is close to the LV. Despite the whole LV is inside the BB, the LV centroid is slightly away from its center.

These SA images typically have 560×560 pixels covering a FOV containing the heart and much more. Reduction of its dimension is an important first step to exclude unnecessary information and speed up the processing tasks. In this work it is presented a fully automated crop function that successfully performed this task over the data from 17 patients.

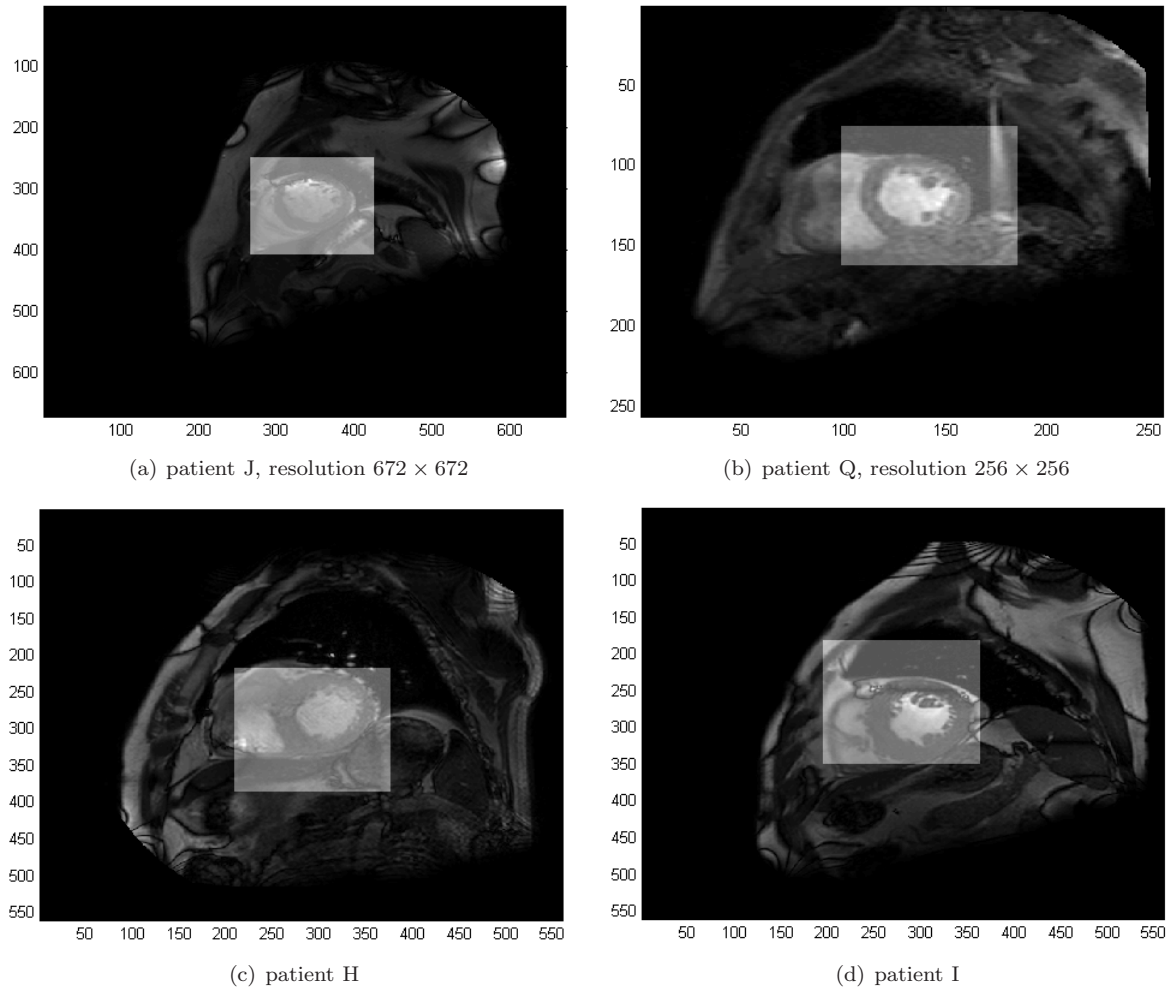

(a) patient J, resolution 672×672

(b) patient Q, resolution 256×256

(c) patient H

(d) patient I

Figure 6.2: Automatic crop results

Alignment-by-reconstruction

The alignment of the planes is needed for an efficient segmentation. Here, a method called *alignment-by-reconstruction* is used, where an intermediate reconstruction step is implemented. Experimental tests were performed with the algorithm here presented: with synthetic and real data.

The synthetic volume has 5 slices. In each slice there is a central circumference and two smaller circumferences placed periferically. The radius of the central circumference increased from slice $1 \rightarrow 5$ and the radius of the smaller ones is fixed. Pseudorandom noise (signal between $[0, 1]$) normally distributed with amplitude of 10% of the signal, *i.e.*, about -10.8dB, was also included.

To simulate the misalignment that can be found in real data, these planes were misaligned with a translation vector randomly generated with normally distributed components (Fig.6.3(a)), with 0 mean and standard deviation σ. The σ represents how much the slice will be misaligned from its original position.

In order to confirm the importance of the reconstruction, the first synthetic tests missed that step. The synthetic data was misaligned with translation vector, generated with $\sigma = 3$ and α was set to 1.5. The results can be compared in Fig.6.3(b) and Fig.6.3(c) and in Table 6.1. The performance of the

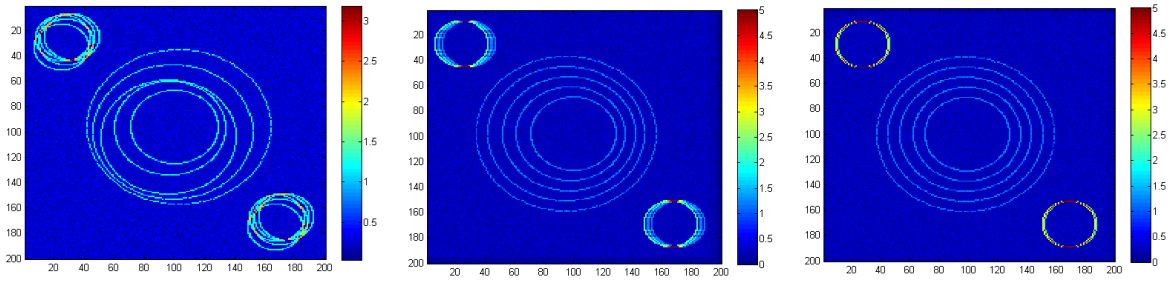

(a) Misaligned synthetic data ($\sigma = 3$) (b) Aligned synthetic data w/o reconstruction (c) Aligned synthetic data w/ reconstruction

Figure 6.3: Alignment results from experimental tests with synthetic data

algorithms was accessed by estimating the error of the translation:

$$\vec{e} \quad = \frac{1}{S} \sum_{s}^{S} T_{original}(s) + T_{estimated}(s). \tag{6.1}$$

Table 6.1: Error of the translation vectors of the experimental results with synthetic data

		$T_{original}(s) + T_{estimated}(s)$	
Plane	Original	w/o Reconstruction	w/ Reconstruction
1	$(-4, 0)$	$(-2, 0)$	$(0, -1)$
2	$(-3, -3)$	$(-2, -2)$	$(0, -1)$
3	$(4, -4)$	$(-2, -3)$	$(0, -2)$
4	$(0, -1)$	$(2, -5)$	$(0, -2)$
5	$(-4, 3)$	$(-2, -5)$	$(0, -2)$
$\|\vec{e}\|$		3.2	0.4

Comparing the translation errors, it is clear that the reconstruction step is essential. The importance of the reconstruction step is based on the information that each plane incorporates about its neighbors (see Fig.6.4). This allows the result to converge in a concentric solution.

Additionally, Monte Carlo tests were performed. For a number of r repetitions, the algorithm was tested for a set of σ (see Eq.6.2). The mean error (Eq.6.3) and standard deviation associated with each σ were estimated. Due to computational limitations, the number of iterations for each σ was not constant:

$$(\sigma, r) = \{(0, 100), (0.1, 100), (0.2, 100), (0.5, 20), (1, 20), (1.5, 20), (2, 10), (2.5, 10)\} \tag{6.2}$$

$$\left\|\vec{\bar{e}}\right\|_{\sigma} \quad = \frac{1}{R} \sum_{r}^{R} \|\vec{e}\|^{r}. \tag{6.3}$$

The results are presented in the graphics in Fig.6.5 and they are encouraging. For lower deviations, the error is really low. However, more iterations are needed to be more conclusive about the performance of the algorithm for higher σ.

In what concerns to the real data, the α parameter was set to 0.9 for all patients. Depending on the amount of data (number of slices mainly), the algorithm could require more iteration steps to converge.

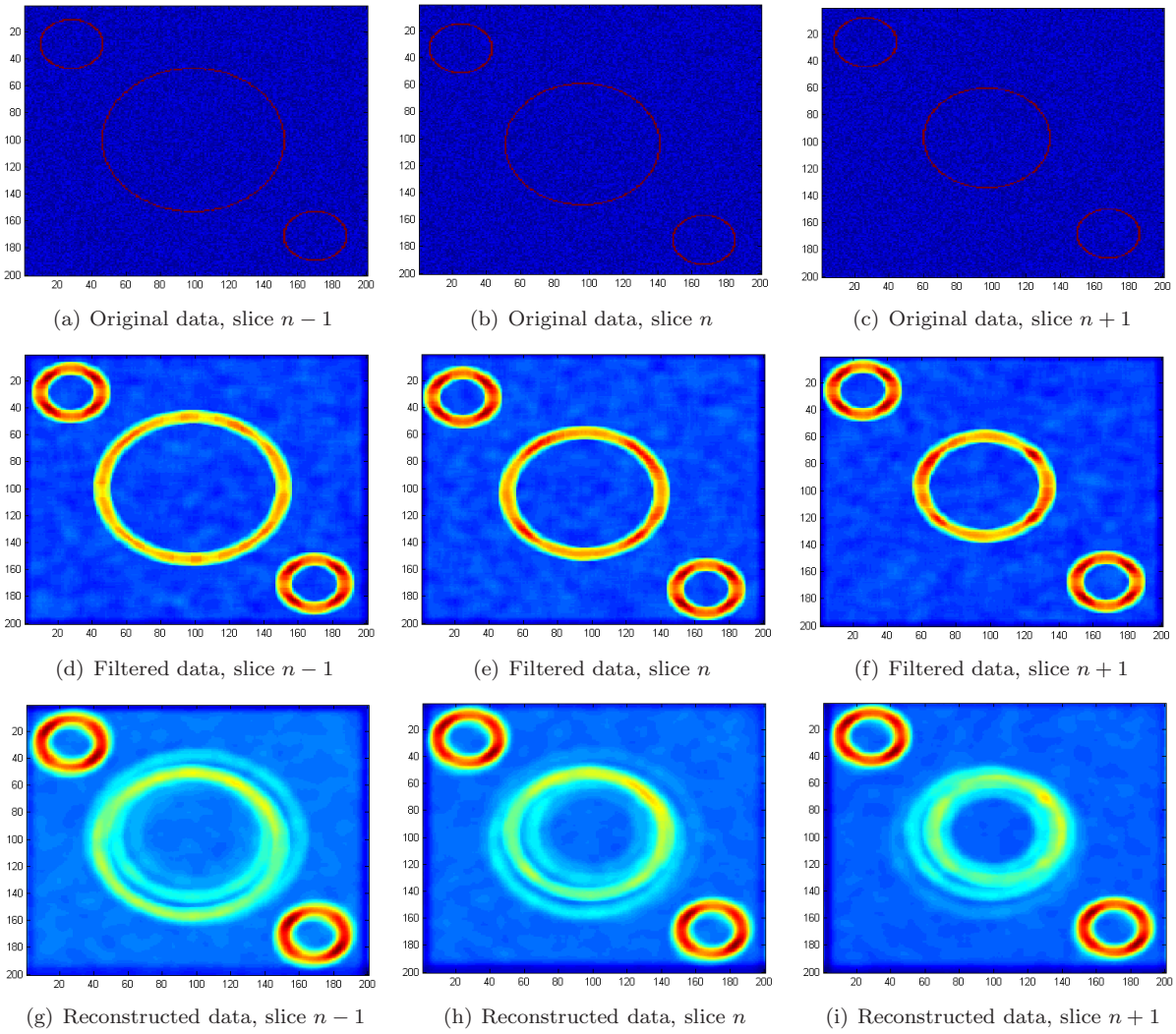

(a) Original data, slice $n-1$ (b) Original data, slice n (c) Original data, slice $n+1$

(d) Filtered data, slice $n-1$ (e) Filtered data, slice n (f) Filtered data, slice $n+1$

(g) Reconstructed data, slice $n-1$ (h) Reconstructed data, slice n (i) Reconstructed data, slice $n+1$

Figure 6.4: Results with synthetic data: importance of the reconstruction step

Here, the performance of the algorithm could only be accessed in a qualitative way, by observing the segmentation results where the deformed contour from slice $s = n$ was used to initialize the neighbor slices $s = n + 1$ if $s > S/2$ or $s = n - 1$ if $s < S/2$ (Fig.6.6(d) to Fig.6.6(f)).

The figures in Fig.6.6 intent to show the importance of the alignment step. From Fig.6.6(a) to Fig.6.6(c) it is possible to observe the contour propagation between consecutive slices without alignment and from Fig.6.6(d) to Fig.6.6(f) the same propagation but with alignment. Based on these observations, it is possible to conclude the importance of the alignment step an automated LV segmentation. The time series were also analyzed and the contour could be propagated without any alignment (Fig.6.6(g) to Fig.6.6(i)). Therefore, the reported artifact induced by the respiratory motion only misaligns the data in the space domain, and that artifact is propagated over the time in a consistent way. The transformation used in the presented images was the one estimated to the slice $s = S/2$.

In the results observed over the 17 patients, the deformed curve in one slice is in general a good initialization for its neighbor, in what depends on the alignment problem (Fig.6.6(d) $\rightarrow$ Fig.6.6(f)). Other problems were found, such as the curve being hold in PM (Fig.6.6(d)), but will only be addressed in the next section. The misalignment is only compensated in the space domain and therefore the estimated

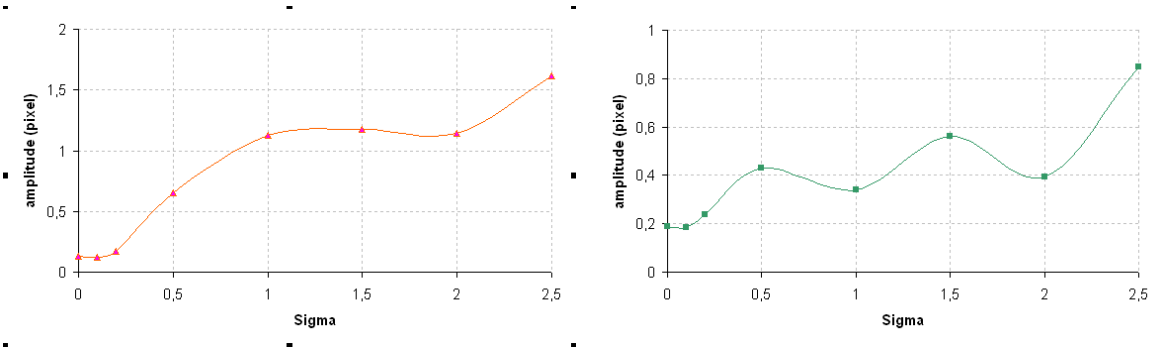

(a) Mean $\|\vec{e}\|_\sigma$ (b) Standard deviation $\|\vec{e}\|_\sigma$

Figure 6.5: Graphics from Monte Carlo results to test the performance of the alignment-by-reconstruction algorithm

translation vector is used across all time courses. The work here presented is an important step toward full automatization of the segmentation of the LV and also represents a novel and innovative approach to this problem.

Segmentation

The core step to estimate the EF, the segmentation, is very sensitive to the initialization despite the great efforts done in this area [22, 49, 50, 23]. Therefore, the automatic initialization is an important step toward full automatization of the LV segmentation.

The contributions of this work toward an automatic LV segmentation end in the initialization algorithm and the expert intervention is still required to tune the segmentation parameters. However, the algorithm was build in such a way that the minimum setup is required. For instance, the parameters responsible for the internal forces α and β are adapted according to the curvature evolution of the neighbor slices previously segmented (see section 5.4).

After proper tunning of the snake parameters, the data from 17 patients was segmented.

Automatic snake initialization

The initialization algorithm was tested over the available patient data. This is the first step where segmentation takes part. Based on the intersecting chords property, a set of points (8 to 16) is estimated and linearly interpolated. This curve with sharp edges (see green dots in Fig.6.7), is the initialization contour for the *snake deformation*, from the middle slice $s = S/2$ and time frame $t = 1$, corresponding to the ED phase. The initialization is considered good once the myocardium border is segmented with the contour (see the *magenta* line in Fig.6.7).

Over all the data, the user intervention was most of the times necessary to manually change the automatic initialization contour into a good initialization. In this step, human intervention is essential since the criteria to segment the myocardium are highly experience-dependent specially due to PM.

This algorithm was tested with two values for the maximum length of the chords: 56mm and 65mm. The first one is the double of the normal maximum radius (see section 3.2) and the second is used to

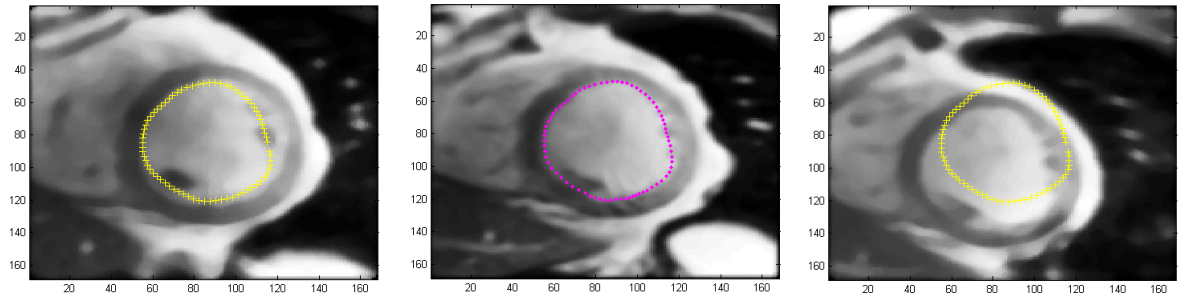

(a) Space series not aligned. $s = S/2-1$ and $t = 1$

(b) Space series initialization not aligned. $s = S/2$ and $t = 1$

(c) Space series not aligned. $s = S/2+1$ and $t = 1$

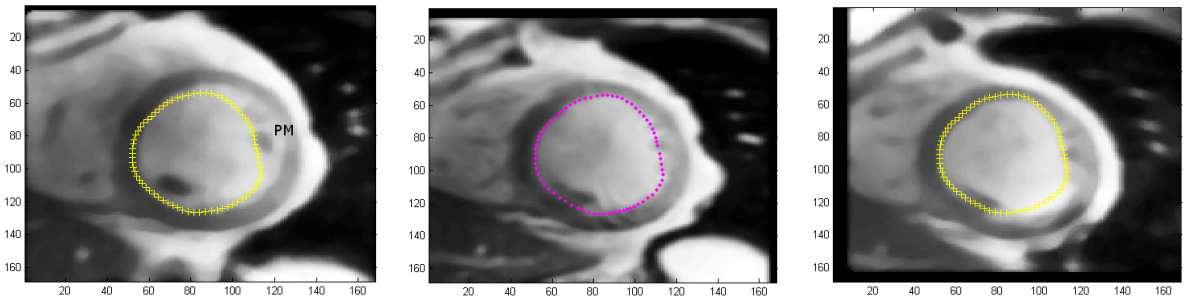

(d) Space series aligned. $s = S/2 - 1$ and $t = 1$

(e) Space series initialization aligned. $s = S/2$ and $t = 1$

(f) Space series aligned. $s = S/2+1$ and $t = 1$

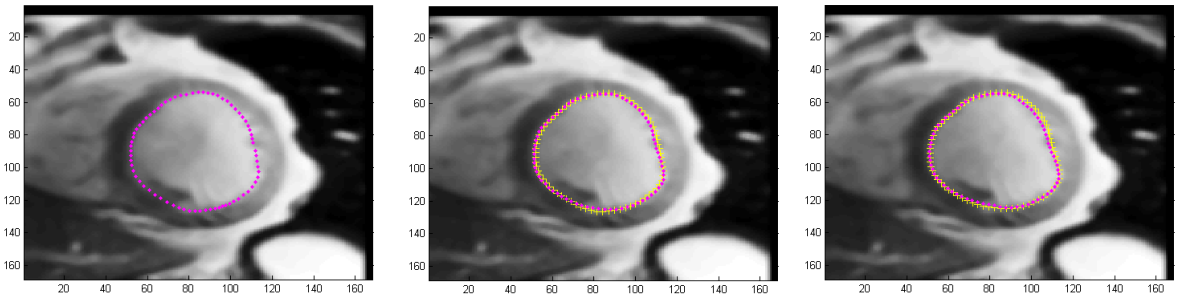

(g) Time series initialization. $s = S/2$ and $t = 1$

(h) Time series. $s = S/2$ and $t = 2$

(i) Time series. $s = S/2$ and $t = 3$

Figure 6.6: Alignment results with real data, Patient A. (*magenta*) contour after segmentation algorithm, (*yellow*) Initialization contour from neighbor plane. It is possible to observe a black frame, caused by the translation.

include pathological dilated hearts. See summary Table 6.2 at the end of this section, the percentage of the segmented contour manually generated.

These two diameters were tested because some difficulties came up, for instance in patients K and N, where the maximum diameter of 56mm was not enough, *i.e.*, there were no sets of chords who fulfilled all the criteria. For this reason, a higher maximum diameter was tested and it performed better in some cases, where probably the heart is dilated. However, in average it performed worse and in two cases the amount of candidate chords caused problems of memory (patients F and O). Therefore, the maximum normal diameter 56mm is the best option.

The best results were observed in patients A, B and D, where human intervention was very small. The PM are responsible for most of the required manual changes (Fig.6.8(a)). They are small structures located in the blood cavity or in the myocardium borders with the same contrast of the myocardium, therefore, their borders might be better ranked than the points resulting from transitions in the endo-

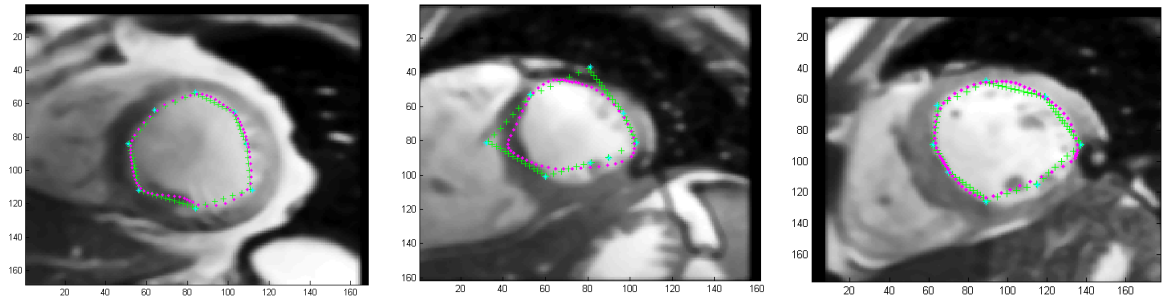

(a) patient A, 22.8% changed (b) patient B, 25.7% changed (c) patient D, 24.6% changed

Figure 6.7: Automatic initialization results. (*blue star*) points from intersecting chords (*green cross*) linear interpolation from the beginning points (*magenta dashed*) contour after segmentation algorithm.

cardium. However, only an expert is qualified to define where the contour should pass, specially when the PM are in the myocardium border (see Fig.6.7 to Fig.6.8 to see different types of PM).

Another problem that affected the performance of the automatic initialization was the centering alteration after the alignment task, presented in Fig.6.8(b). This happened with the patient K. In this patient, there was no set of initialization points that fulfill the requirements, and therefore the initialization has to be performed completely manually.

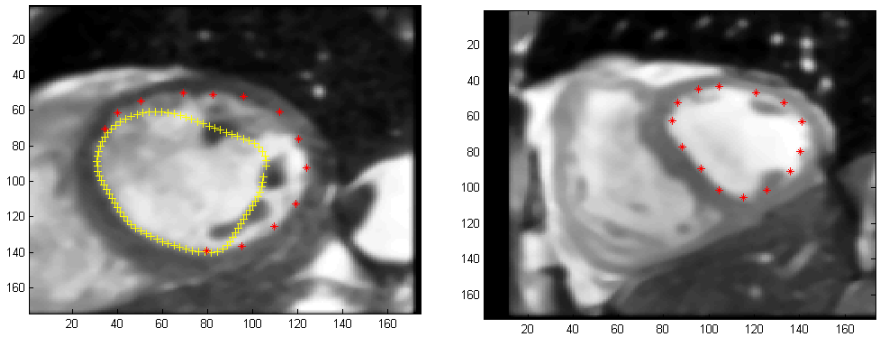

(a) Papillary muscles, patient N (b) Bad centering after alignment, patient L

Figure 6.8: Automatic initialization results: difficulties. (*magenta*) contour after segmentation algorithm, (*yellow*) Initialization contour, (*red*) manual changing a segment of the contour.

For each patient, the segmentation parameters were tunned. The setup parameters are listed in the summary table presented in the end of this section. Most of the patients could be grouped with similar parameters. The ideal contour estimated from this step is used to initialize the contours for both time and space segmentation, as described in the next sections.

ESF estimation

With the correct setup of the segmentation parameters, the ESF was automatically estimated for most of the patients (9 out of 17). The initialization for the ESV estimation was also estimated in this step, where 7 out of 17 were correctly automatically segmented. The estimated ESF are listed in Table 6.2 along with the correct ESF. An example is showed in Fig.6.9.

Analyzing the results presented in Table 6.2, in most of the cases where the ESF is miss-estimated,

the error is normally of 1 time frame (exception for patients N and P).

The segmentation in the time domain is less prone to difficulties since the temporal resolution is generally high and the transition between frames is smooth. However, the PM might introduce error in the ESF estimation or in ESF segmentation (see Fig.6.10) and there are difficulties when the cavity at the ESF is very small. Therefore, the expert supervision is very important.

The segmentation of the time series was also used to prove the hypothesis assumed that the first time frame corresponded to the ED phase. The area of the frame $t = T$ was smaller that $t = 1$ for all the tested patients. Additionally, when the estimated ESF is about half of the time course, it can be an indication for taquicardia.

Snake deformation

In the last step of the segmentation process, the ED and ES volumes are segmented. For every patient, the set of segmentation parameters was tunned for both phases (see Table 6.3). For some patients, the same set was used for both cardiac phases.

Thanks to the alignment step, the contour propagation method worked successfully in most of cases. However, two main difficulties came up: (i) the PM stopped the evolution of the snake into the myocardium and (ii) the abrupt radius variation of the LV section at the appex did not allowed the use of the neighbor contours in these cases. Fortunately, in most of the cases these are also the disposable slices, where there was no LV left or did not fulfill the criteria to be accounted to the EF estimation (see section 1.2).

In figures Fig.6.11 to Fig.6.12 it is presented the segmentation results from patient G. The set of planes $\{8, 9, 10, 11, 12, 13\}$ do not fulfill the requirements to estimate the EF. The contour propagation in the middle planes is smooth. However, closer to the appical planes the PM increase their influence and the results have to be manually changed. The LV radius decrease from $3 \rightarrow 4$ is high and therefore the segmentation is poorer.

In the presented example, the diastolic slices required no changes in $6, 7$, minor changes in $4, 5$ and major interventions in $1, 2, 3$. The systolic slices required no changes in $3, 6, 7$, minor changes in 4 and major interventions in $1, 2, 5$. Once the segmentation parameters can be automatically setup, these results represent great improvement to the clinical routine, because only minor changes have to be performed by the expert.

These results were inspected by an expert and the EF was estimated and compared with the software in the workstation. The main difficulties found in the presented solution concern the user interface, where zooming and contrast change is no option. Therefore, the manual changes introduced have low reproducibility. The software result was $EF = 63\%$ and the presented algorithm showed values between 62% and 67%.

Table 6.2: Summary of main results. (T) when no initialization is automatically suggested. (OOM) Out of memory. (^{1}) manual identification of the ESF. (^{2}) manual change of the contour of the ESF

Patient	Crop Reduction	Change Initialization		ESF	
		56mm	65mm	Estimated	Correct
A	30.0%	22.8%	21.7%	14	14
B	30.5%	25.7%	50.0%	7	7
C	30.0%	38.7%	100.0%	$8^{(1,2)}$	9
D	32.4%	24.6%	50.1%	14^2	14
E	28.1%	T	61.0%	12	12
F	30.0%	$(32.7 + 32.9)\%$	OOM	$12^{(1,2)}$	13
G	30.0%	$(33.7 + 30.9)\%$	$(29.9 + 14.6)\%$	12^2	12
H	30.0%	71.1%	56.8%	$10^{(1,2)}$	9
I	30.0%	$(49.4 + 18.9)\%$	$(25.0 + 60.0)\%$	$12^{(1,2)}$	13
J	25.4%	32.1%	$(14.4 + 29.7)\%$	14	14
K	26.3%	T	T	13^2	13
L	30.0%	62.8%	$(39.1 + 25.8)\%$	13	13
M	30.0%	48.8%	65.1%	10	10
N	30.0%	T	61.5%	$8^{(1,2)}$	13
O	30.2%	64.9%	OOM	9	9
P	30.0%	53.6%	87.4%	$13^{(1,2)}$	15
Q	34.0%	71.1%	$(8.5 + 57.0)\%$	$12^{(1,2)}$	12
Mean $\pm$ STD	29.8 ± 1.9	55.5 ± 29.0	68.1 ± 23.6		

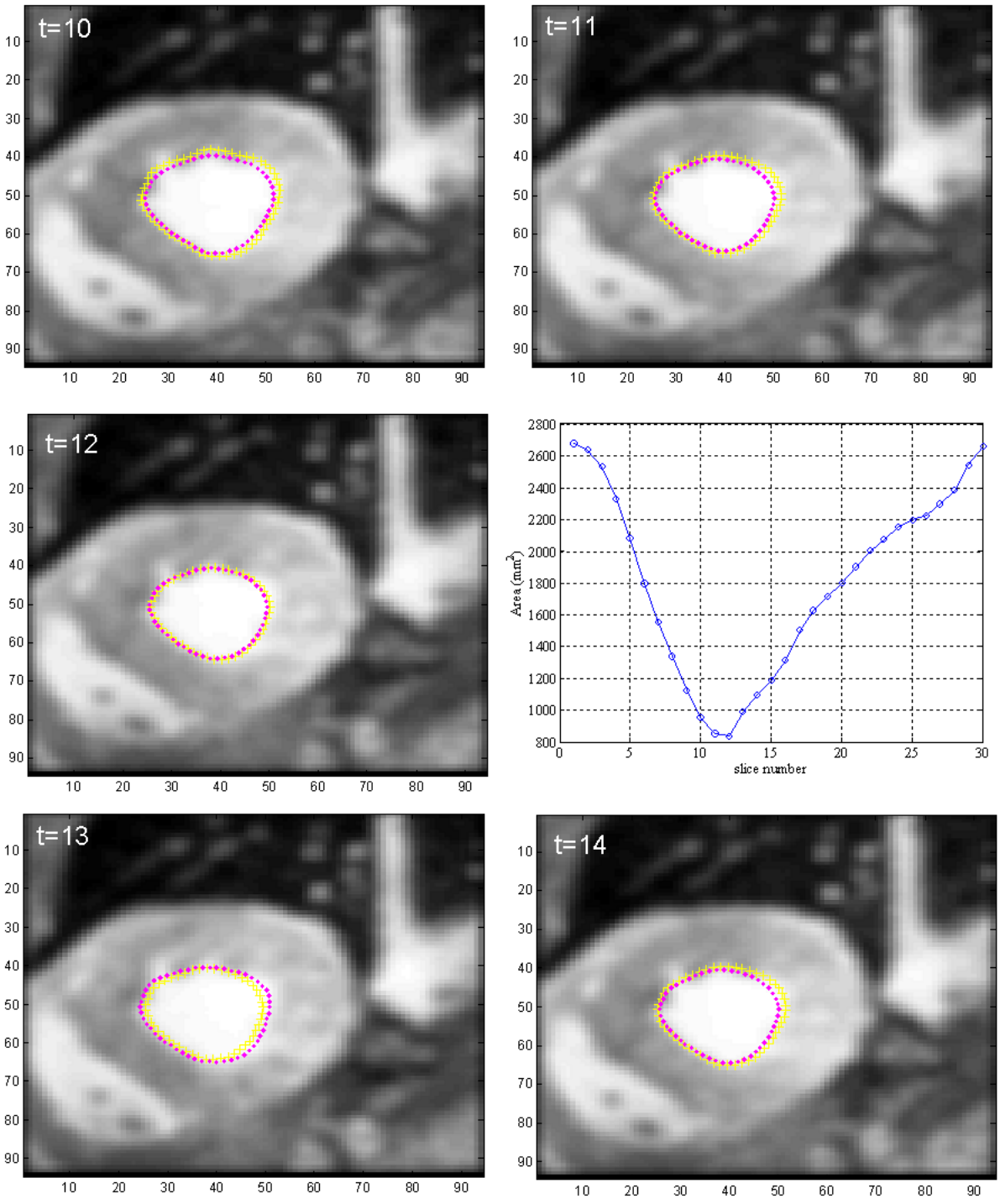

Figure 6.9: Segmented time series around the ESF, patient E. (*yellow cross*) linear interpolation from the beginning points (*magenta dashed*) contour after segmentation algorithm (*graphic*) area estimation over all time series.

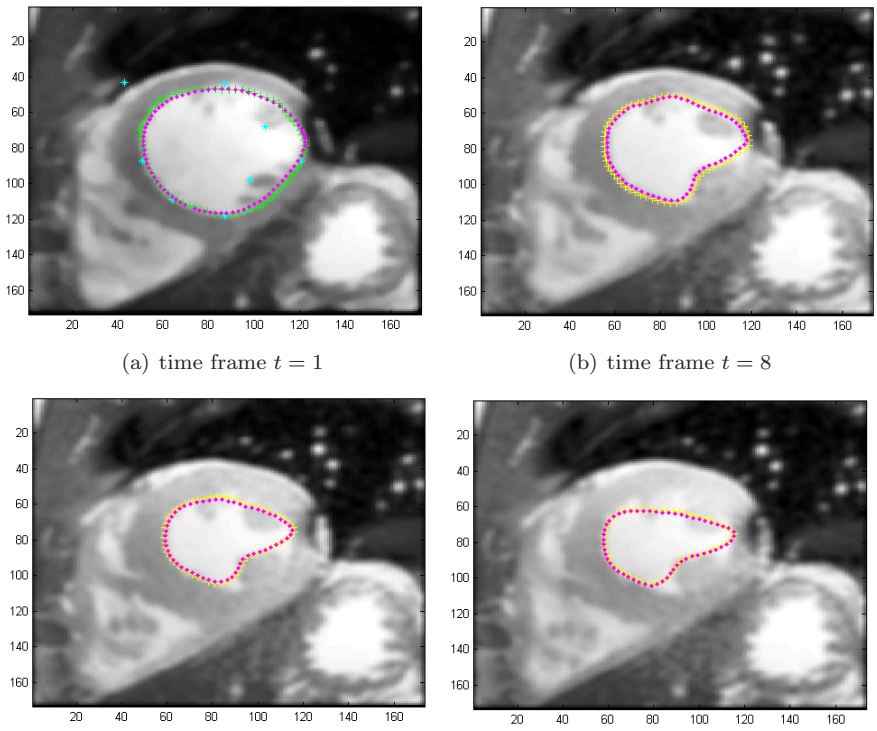

(a) time frame $t = 1$ (b) time frame $t = 8$

(c) time frame $t = 12$ (d) time frame $t = 15$

Figure 6.10: ESF estimation, patient P. (*magenta*) contour after segmentation algorithm, (*yellow*) Initialization contour.

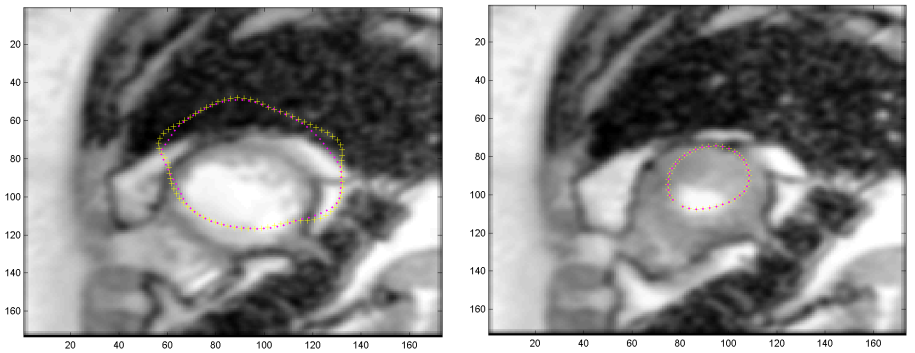

(a) Diastole, slice 2

(b) Systole, slice 2

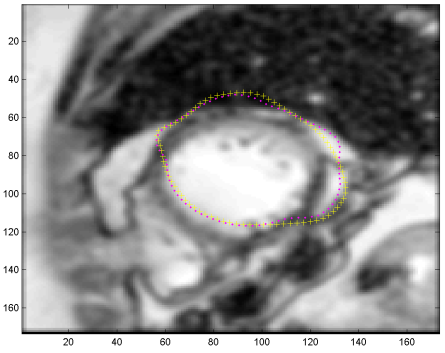

(c) Diastole, slice 3

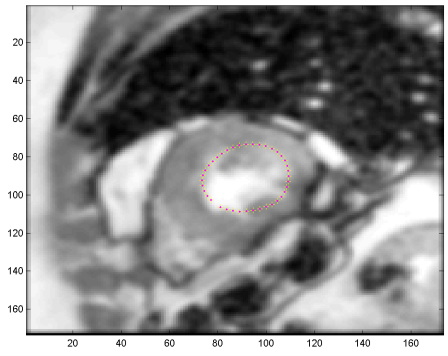

(d) Systole, slice 3

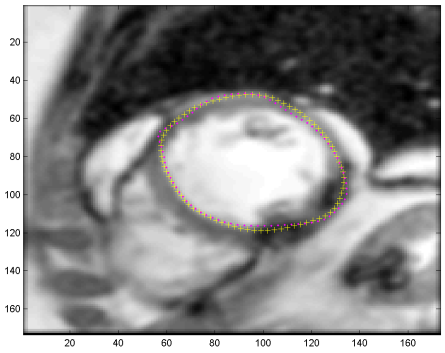

(e) Diastole, slice 4

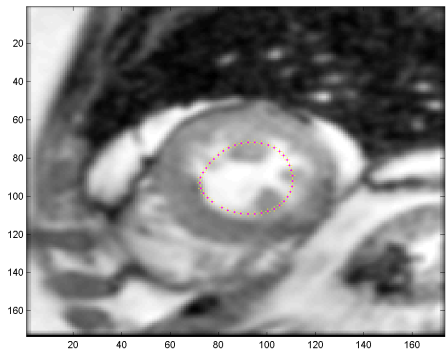

(f) Systole, slice 4

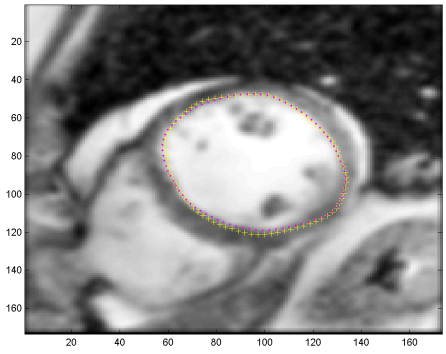

(g) Diastole, slice 5

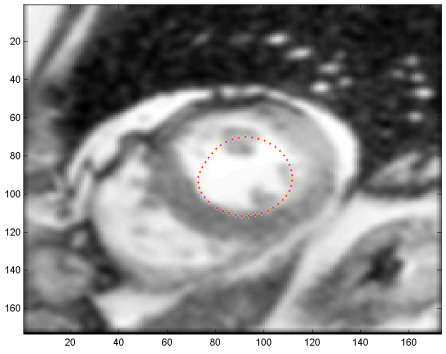

(h) Systole, slice 5

Figure 6.11: Segmentation results, slice 2 to 5, patient G. (*magenta*) contour after segmentation algorithm, (*yellow*) Initialization contour.

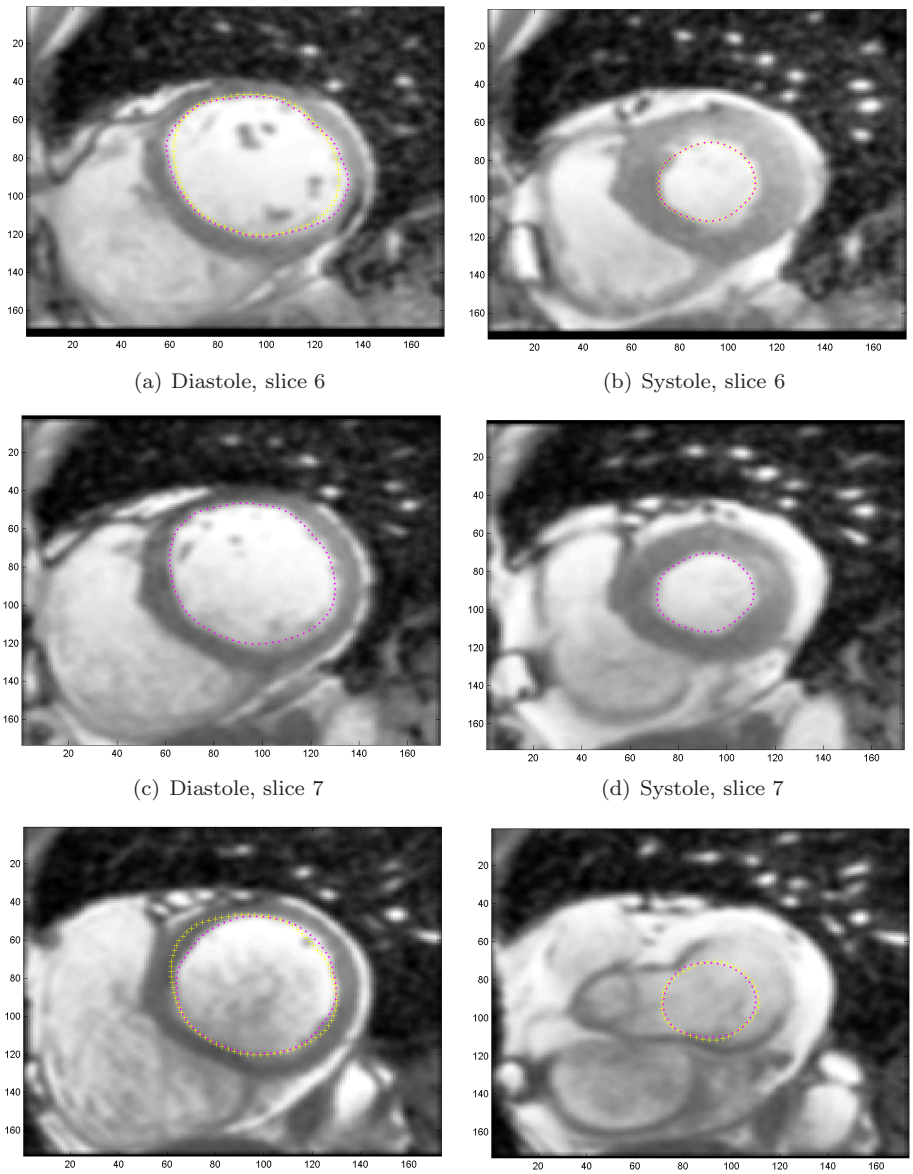

(a) Diastole, slice 6

(b) Systole, slice 6

(c) Diastole, slice 7

(d) Systole, slice 7

(e) Diastole, slice 8

(f) Systole, slice 8

Figure 6.12: Segmentation results, slice 6 to 8, patient G. (*magenta*) contour after segmentation algorithm, (*yellow*) Initialization contour.

Table 6.3: Summary of segmentation parameters. (*Ini*) Initialization parameters. (*T*) Time series parameters. (*S ED*) Space, end diastolic parameters. (*S ES*) Space, end systolic parameters.

		A	B	C	D	E	F	G	H	I	J	K	L	M	N	O	P	Q
Ini	α	0.03	0.03	0.03	0.03	0.5	0.03	0.5	0.8	0.5	0.5	0.5	0.5	0.5	0.6	0.5	0.8	0.5
	β	0.1	0.6	0.3	0.3	0.2	0.1	0.7	0.8	0.7	0.7	0.7	0.7	0.7	0.8	0.5	0.8	0.7
	γ	15	1	10	10	30	10	25	25	25	15	30	15	15	15	25	25	30
	k	25	25	25	25	30	25	50	80	50	70	50	70	50	50	50	50	50
T	α	0.05	0.5	0.08	0.7	0.3	0.07	0.5	0.3	0.5	0.5	0.4	0.4	0.6	0.4	0.4	0.4	0.08
	μ_α	1	1	1	1	1	1	0.3	1	1	0.5	1	1	1	1	1	1	1
	β	0.3	0.2	0.1	0.3	0.1	0.1	0.4	0.4	0.3	0.5	0.4	0.4	0.6	0.3	0.4	0.4	0.08
	μ_β	1	1	1	1	1	1	1	1	1	0.5	1	1	1	1	1	1	1
	γ	20	30	30	40	30	30	40	30	25	25	40	30	35	30	30	30	40
	k	80	180	180	300	100	300	220	300	350	250	300	320	200	300	300	300	200
S ED	α	0.2	0.3	0.3	0.4	0.4	0.1	0.4	0.4	0.5	0.2	0.5	0.5	0.4	0.4	0.4	0.4	0.2
	β	0.1	0.1	0.1	0.4	0.4	0.1	0.3	0.4	0.5	0.2	0.5	0.4	0.4	0.4	0.4	0.4	0.2
	γ	15	10	10	30	30	20	35	20	30	30	30	30	30	30	30	30	20
	k	100	140	140	300	100	250	220	250	300	300	300	220	250	250	300	300	200
S ES	α	0.01	0.3	0.3	0.4	0.4	0.05	0.05	0.05	0.3	0.2	0.3	0.5	0.4	0.4	0.4	0.4	0.1
	β	0.1	0.1	0.1	0.4	0.4	0.05	0.1	0.1	0.3	0.2	0.3	0.4	0.4	0.4	0.4	0.4	0.1
	γ	10	10	10	25	25	30	30	30	30	30	30	30	30	30	30	25	20
	k	100	140	140	370	170	300	300	300	300	300	300	220	250	250	300	270	200

Chapter 7

Conclusions

The LV function analysis is currently performed manually in the clinical routine in a labor, time-consuming, operator biased task. In most of the proposed algorithms only a part of the stated difficulties are addressed. Normally, the alignment problem is hardly addressed and few give robust solutions concerning the signal variation over the slice and over the different image planes. Attending to these considerations, no fully automatic initialization is achieved using a single view of the LV.

According to this lack, a new approach must be used, combining most of the proposed models and methodologies and attending to all the SA cine-MR difficulties in order to achieve an improved, robust and fully automated LV segmentation.

In this thesis a set of contributions are proposed toward a fully automatic LV segmentation from SA cine-MR images. Mainly, an algorithm for automatic cropping and another for intra-plane alignment. Additionally, algorithms for automatic snake initialization and ESF estimation were also implemented.

The huge amount of data usually available in cardiac imaging may be reduced because the useful information for LV tracking can be found in a small ROI. The *automatic crop* algorithm aims at discarding the unnecessary information to reduce the amount of data to be processed. Based on the HT, this algorithm is able to robustly reduce the image size for all the data-set tested to about 30% of the original size, reducing the computation burden for the tasks that follow.

The other main contribution is the alignment procedure, that aim at compensating for displacements caused by heart displacement over the several breath-hold periods required during the acquisition process. This may lead to inconsistencies on the reconstructed volume from which the LV is segmented.

The proposed alignment algorithm uses a reconstructed volume to perform the alignment. In the reconstruction step, the energy of a given slice is diffused into its neighbors. With this strategy, a global alignment involving all images on the stack volume is performed without the need of a reference image. The so called *alignment-by-reconstruction* algorithm had encouraging results with the synthetic data, highlighting the importance of the reconstruction step. With the real data, the observed results were also important, they allowed an efficient propagation of the deformable contours into the neighbor slice.

Finally, a segmentation algorithm based on snakes and GVF was implemented. The initialization of the snake is very important to the success of the segmentation, therefore the *automatic snake initial-*

ization algorithm was implemented. Although it showed some limitations due to the papillary muscles, it represents a refreshing contribution to solve this problem because the expert intervention is generally smaller.

The ESF was also successfully identified for most of the patients (9 out of 17), however it is quite sensitive to the correct tunning of the segmentation parameters.

A full volume segmentation is also implemented. The major limitation here is the setup of the segmentation parameters. This difficulty can be overcome with future work, introducing shape information and reducing the importance of the internal forces. However, the importance of this step is to validate the previously described algorithms, that represent a great contribution toward a fully automatic LV segmentation.

Future work

- Explore the adaptive windowing in the *automatic crop* algorithm.
- Use of fuzzy theory to identify the blood-pool, as suggested in [21].
- Include shape information and use 3-D model to decrease the influence of the internal forces and of the PM.
- Automatically exclude spurious slices from EF estimation.
- Create a robust user interface with basic image analysis tools such as zooming, change contrast, etc.
- Increase the data-set and perform tests to compare the time efficiency and the EF value with the software available in the clinical routine.

Appendix

Detailed data information

Table 7.1: Detailed data information. (s) number of slices, (t) number of time frames.

Patient	s	t	s×t	FOV	Resolution(mm)	TR (ms)	TE (ms)	FA
A	10	30	300	560×560	0.73	4.1	2.0	45°
B	14	20	280	512×512	0.78	4.0	2.0	45°
C	12	30	360	560×560	0.73	4.1	2.0	45°
D	12	30	360	528×528	0.71	4.1	2.0	45°
E	15	30	450	320×320	1.34	4.4	2.6	15°
F	11	30	330	560×560	0.73	4.0	2.0	45°
G	10	30	300	560×560	0.73	4.1	2.0	45°
H	9	30	270	560×560	0.73	4.0	2.0	45°
I	11	30	330	560×560	0.73	4.0	2.0	45°
J	10	30	300	672×672	0.71	4.2	2.1	45°
K	12	30	360	560×560	0.73	4.1	2.1	45°
L	14	30	420	560×560	0.73	4.1	2.0	45°
M	12	30	360	560×560	0.73	4.1	2.0	45°
N	14	30	420	640×640	0.72	4.5	2.2	45°
O	11	15	160	576×576	0.69	4.2	2.1	45°
P	12	30	360	560×560	0.73	4.7	2.4	45°
Q	10	30	300	256×256	1.41	4.3	2.5	15°

Int. J. of Tomography & Statistics, Special Issue on Image Processing (accepted)

Bibliography

[1] J. Sanches and J. S. Marques, "Joint image registration and volume reconstruction for 3d ultrasound," Pattern Recognition Letters, vol. 24, pp. 791–800, 2003.

[2] WHO, "Cardiovascular diseases, fact sheet nr. 137," Online, World Health Organization, February 2007.

[3] A. F. Fragi, W. J. Niessen, and M. A. Viergever, "Three-dimensional modeling for functional analysis of cardiac images: review," IEEE transactions on medical imaging, vol. 20, no. 1, pp. 2–25, January 2001.

[4] K. Wu and J. Lima, "Noninvasive imaging of myocardial viability: current techniques and future developments," Circulation Research, vol. 93, pp. 1146–1158, December 2003.

[5] J. A. C. Lima and M. Y. Desai, "Cardiovascular magnetic resonance imaging: current and emerging applications," Journal of the American College of Cardiology, vol. 44, no. 6, pp. 1164–71, September 2004.

[6] C. B. Higgins and H. Sakuma, "Heart disease: Functional evaluation with mr imaging," Radiology, vol. 199, pp. 307–315, May 1996.

[7] G. Constantine, K. Shan, S. D. Flamm, and M. U. Sivananthan, "Role of mri in clinical cardiology," The Lancet, vol. 363, pp. 2162–71, June 2004.

[8] task force of the European Society of cardiology in collaboration with the Association of European Paediatric cardiologists, "The clinical role of magnetic resonance in cardiovascular disease," European Heart Journal, vol. 19, pp. 19–39, 1998.

[9] A. J. Duerinckx, "Cardiac mri for clinicians: an overview," The International Journal of Cardiovascular Imaging, vol. 17, pp. 437–443, 2001.

[10] A. C. Larson, P. Kellman, A. Arai, G. A. Hirsch, E. McVeigh, D. Li, and O. P. Simonetti, "Preliminary investigation of respiratoty self–gating for free–breathing segmented cine mri," Magnetic Resonance in Medicine, vol. 53, no. 1, pp. 159–168, January 2005.

[11] L. Baboi, L. Milot, C. Lartizien, C. Roche, J. Y. Scoazec, F. Pilleul, and O. Beuf, "Synchronisation strategies in t2-weighted mr imaging for detection of liver lesions: Application on a nude mouse model," Biomedical Imaging and Intervention Journal, vol. 3, no. 4, 2007.

[12] M. D. Cerqueira, N. J. Weissman, V. Dilsizian, A. K., Jacobs, S. Kaul, W. K. Laskey, D. J., Pennell, J. A. Rumberger, T. Ryan, M. S. Verani, A. H. A. W. G. on Myocardial Segmentation, and R. for Cardiac Imaging, "Standardized myocardial segmentation and nomenclature for tomographic imaging of the heart: A statement for healthcare professionals from the cardiac imaging committee of the council on clinical cardiology of the american heart association," Journal of Nuclear Cardiology, vol. 9, no. 2, pp. 240–245, 2002.

[13] R. I. Pettigrew, J. N. Oshinski, G. Chatzimavroudis, and W. T. Dixon, "Mri techniques for cardiovascular imaging," Journal of Magnetic Resonance Imaging, vol. 10, pp. 590–601, 1999.

[14] A. Holland, J. Goldfarb, and R. Edelman, "Diaphragmatic and cardiac motion during suspended breathing: preliminary experience and implications for breath–hold mr imaging," Radiology, vol. 209, no. 2, pp. 483–489, November 1998.

[15] K. McLeish, D. Hill, D. Atkinson, J. Blackall, and R. Razavi, "A study of the motion and deformation of the heart due to respiration," Medical Imaging, IEEE Transactions on, vol. 21, no. 9, pp. 1142–1150, Sep 2002.

[16] A. Pednekar, R. Muthupillai, V. Lenge, I. Kakadiaris, and S. Flamm, "Automatic identification of the left ventricle in cardiac cine-mr images: Dual-contrast cluster analysis and scout-geometry approaches," Journal of Magnetic Resonance Imaging, vol. 23, pp. 641–651, April 2006.

[17] T. D. Karamitsos, L. E. Hudsmith, J. B. Selvanayagam, S. Neubauer, and J. M. Francis, "Operator induced variability in left ventricular measurements with cardiovascular magnetic resonance is improved after training," Journal of Cardiovascular Magnetic Resonance, vol. 9, no. 5, pp. 777–783, September 2007.

[18] D. L. Pham, C. Xu, and J. L. Prince, "Current methods in medical image segmentation," Annual Review Biomedical Engineering, vol. 2, pp. 315–337, 2000.

[19] T. McInerney and D. Terzopoulos, "Deformable models in medical image analysis: a survey," Medical Image Analysis, vol. 1, no. 2, pp. 91–108, 1996.

[20] A. Katouzian, A. Prakash, and E. Konofagou, "A new automated technique for left- and right-ventricular segmentation in magnetic resonance imaging," Engineering in Medicine and Biology Society, 2006. EMBS '06. 28th Annual International Conference of the IEEE, pp. 3074–3077, September 2006.

[21] A. Pednekar and I. Kakadiaris, "Image segmentation based on fuzzy connectedness using dynamic weights," Image Processing, IEEE Transactions on, vol. 15, no. 6, pp. 1555–1562, June 2006.

[22] M. Kass, A. Witkin, and D. Terzopoulos, "Snakes: Active contour models," International Journal of Computer Vision, pp. 321–331, 1988.

[23] C. Xu and J. L. Prince, "Snakes, shapes, and gradient vector flow," IEEE Transactions on Image Processing, vol. 7, no. 3, pp. 359–369, March 1998.

[24] W. Sorgel and V. Vaerman, "Automatic heart localization from a 4d mri dataset," in Proc. of the SPIE Conference on Medical Imaging, 1997, pp. 333–344.

[25] V. Medina, R. Valdes, and O. Yanez-Suarez, "Automatic initialization for a snakes-based cardiac contour extraction," in Proc. of 22nd Annual Int. Conf IEEE-EMBS Chicago IL, Jully 2000, pp. 1625–1628.

[26] V. Medina, M. Garza, J. Lerallut, P. Meer, O. Yanez-Suarez, and R. Valdes, "Robust segmentation of the left ventricle from mri," Engineering in Medicine and Biology Society, 2003. Proceedings of the 25th Annual International Conference of the IEEE, vol. 1, pp. 611–613, September 2003.

[27] X. Huang, D. Metaxas, and T. Chen, "Metamorphs: Deformable shape and texture models," in Computer Vision and Pattern Recognition, 2004. CVPR 2004. Proceedings of the 2004 IEEE Computer Society Conference on, vol. 1, June-2 July 2004, pp. 496–503.

[28] D. Metaxas, T. Chen, X. Huang, and L. Axel, "Metamorphs: Deformable shape and texture models," in 8th WSEAS International Conf. on Computers, special session on Imaging and Image Processing of Dynamic Processes in biology and medicine, WSEAS Transactions, Athens, Greece, July 2004.

[29] P. Clarysse, D. Friboulet, and I. Magnin, "Tracking geometrical descriptors on 3-d deformable surfaces: application to the left-ventricular surface of the heart," Medical Imaging, IEEE Transactions on, vol. 16, no. 4, pp. 392–404, Aug 1997.

[30] J. Canny, "A computational approach to edge detection," Pattern Analysis and Machine Intelligence, IEEE Transactions on, vol. PAMI-8, no. 6, November 1986.

[31] A. F. Frangi, D. Rueckert, J. A. Schnabel, and W. J. Niessen, "Automatic construction of multiple-object three-dimensional statistical shape models: application to cardiac modeling," IEEE Transactions on Medical Imaging, vol. 21, no. 9, pp. 1151–1166, September 2002.

[32] S. C. Mitchell, J. G. Bosch, B. P. F. Lelieveldt, R. J. van der Geest, J. H. C. Reiber, and M. Sonka, "3-d active appearance models: segmentation of cardiac mr and ultrasound images," IEEE Transactions on Medical Imaging, vol. 21, no. 9, pp. 1167–78, September 2002.

[33] C. Pluempitiwiriyawej, J. M. F. Moura, Y.-J. L. Wu, and C. Ho, "Stacs: New active contour scheme for cardiac mr image segmentation," IEEE Transactions on Medical Imaging, vol. 24, no. 5, pp. 593–603, May 2005.

[34] Q. Chen, Z. M. Zhou, M. Tang, P. A. Heng, and D.-S. Xia, "Shape statistics variational approach for the outer contour segmentation of the left ventricle mr images," IEEE Transactions on Information technology in biomedicine, vol. 10, no. 3, pp. 588–597, July 2006.

[35] L. Cordero-Grande, P. Casaseca-de-la Higuera, M. Martin-Fernandez, and C. Alberola-Lopez, "Endocardium and epicardium contour modeling based on markov random fields and active contours," Engineering in Medicine and Biology Society, 2006. EMBS '06. 28th Annual International Conference of the IEEE, pp. 928–931, September 2006.

[36] S. Zambal, J. Hladuvka, and K. Bühler, "A fully automatic system for segmentation and analysis of the left and right ventricles of the heart using a bi-temporal two-component model," Computer Assisted Radiology and Surgery, pp. 93–94, 2007.

[37] Y. Zhu, P. Yan, X. Papademetris, A. Sinusas, and J. Duncan, "Integrated segmentation and deformation analysis of 4-d cardiac mr images," Biomedical Imaging: From Nano to Macro, 2008. ISBI 2008. 5th IEEE International Symposium on, pp. 1437–1440, May 2008.

[38] J. Nascimento and J. Sanches, "Ultrasound imaging lv tracking with adaptive window size and automatic hyper-parameter estimation," in Proceedings IEEE ICIP 2008. San Diego, California, U.S.A: 2008 IEEE International Conference on Image Processing, October 1215 2008.

[39] C. A. Cocosco, T. Netsch, J. Sénégas, D. Bystrov, W. J. Niessen, and M. A. Viergever, "Automatic cardiac region-of-interest computation in cine 3d structural mri," CARS, pp. 1126–1131, 2004.

[40] A. Müller, A. Neitmann, N. Merkle, J. Wohrle, V. Hombach, and H. Kestler, "Contour detection of short axis slice mr images for contraction irregularity assessment," Computers in Cardiology, pp. 21–24, 2005.

[41] P. V. C. Hough, "Method and means of recognizing complex patterns," Patent 3 069 654, 1962.

[42] D. H. Ballard, "Generalizing the hough transform to detect arbitrary shapes," Pattern Recognition, vol. 13, no. 2, pp. 111–122, 1981.

[43] H. Feigenbaum, Feigenbaum's echocardiography. Philadelphia: PA: Lippincott, 2005.

[44] T. Makela, P. Clarysse, O. Sipila, N. Pauna, Q. C. Pham, T. Katila, and I. E. Magnin, "A review of cardiac image registration methods," IEEE Transactions on Medical Imaging, vol. 21, no. 9, pp. 1011–1021, September 2002.

[45] K. S. Shriram, S. Suryanarayanan, V. Vaidya, and R. Srinivasan, "Unbiased multipli-subject alignment of left ventricles," in Proceedings IEEE ISBI 2008. Paris, France: 2008 5^{th} IEEE International Symposium on Biomedical Imaging: From Nano to Macro, May 1417 2008.

[46] S. Zambal, J. Hladuvka, and K. Bühler, "Improving segmentation of the left ventricle using a two-component statistical model," in Proceedings of Medical Image Computing and Computer-Assisted Intervention (MICCAI), 2006, pp. 151–158.

[47] B. M. Dawant and A. P. Zijdenbos, "Image segmentation," in Handbook on Medical Imaging - Volume II: Medical Image Processing and Analysis, J. M. Fitzpatrick and M. Sonka, Eds. SPIE Press Monograph Vol. PM80, 2000.

[48] C. Xu, D. L. Pham, and J. L. Prince, "Image segmentation using deformable models," in Handbook on Medical Imaging - Volume II: Medical Image Processing and Analysis, J. M. Fitzpatrick and M. Sonka, Eds. SPIE Press Monograph Vol. PM80, 2000.

[49] L. D. Cohen, "On active contour models and ballons," Computer Vision, Graphics and Image Processing: Image Understanding, vol. 53, no. 2, pp. 211–218, 1989.

[50] L. D. Cohen and I. Cohen, "Finite-element methods for active contour models and balloons for 2-d and 3-d images," IEEE Transactions on Pattern analysis and machine intelligence, vol. 15, no. 11, pp. 1131–1147, November 1993.

[51] H.-S. Kim and J.-H. Kim, "A two-step circle detection algorithm from the intersecting chords," Pattern Recognition Letters, vol. 22, pp. 787–798, 2001.

[52] W. F. Ganong, "The heart as a pump," in Review of Medical Physiology (LANGE Basic Science), 20^{th} edition, J. M. Fitzpatrick and M. Sonka, Eds. McGraw-Hill Medical, 2001.

Automatic Cropping for LV Segmentation in Cardiac MRI

Isabela Silva[1]*, Ana G. Almeida[2] and João Sanches[1]

[1]Institute for Systems and Robotics
Instituto Superior Técnico
1049-001 Lisbon, Portugal

[2]Faculdade de Medicina da Universidade de Lisboa
1649-028 Lisbon, Portugal

ABSTRACT

Left ventricle (LV) contour extraction and tracking is important in diagnosis of cardiac pathologies. This procedure is difficult, is usually performed manually using software assistance, is time consuming and presents high intra/inter operator variability. Automatization of this process is of great importance to the clinical practice.

The most state of the art algorithms for LV segmentation, described in the literature, are semi-automatic allowing to reduce significantly the human intervention. A full automatic approach is still an open problem mainly because it is difficult to compute a good initial guess for the contour, close enough of the final solution. Additionally, since the total amount of available data is usually large, and the *region of interest* (ROI) containing the LV is smaller than the overall acquired volume, an automatic crop is needed to reduce the computational burden associated with the pre-processing and segmentation algorithms. The pre-processing performs compensation in one hand, for coil sensitivity that induces intensity fluctuations across the images and, in the other hand, for misalignments due small movements during the breath-hold acquisition protocol.

In this paper we propose an algorithm to automatically crop the acquired volume by defining an adaptive size ROI containing the LV. This cropping is based on the well known Hough transform for circles, in the prior knowledge about the location of the heart and also on the high signal variability over time due to muscle contraction at the LV borders.

Tests with real data have shown promising results.

Keywords: left ventricle, automatic crop, Hough transform.

1 Introduction

There are several non-invasive imaging techniques available to assess myocardial function, such as *echocardiography*, *single photon emission computed tomography* (SPECT), *positron emission tomography* (PET) and Magnetic Resonance Imaging (MRI).
MRI is one of the preferred diagnostic technique due to its high spatial resolution and soft-tissue contrast. Furthermore, despite the structural information, such as anatomy and tissue

*Corresponding author: Isabela Silva (isabela.silva@ist.utl.pt)

characterization, it provides the dynamic analysis such as perfusion, metabolism and function measurements in one single examination (Wu and Lima, 2003).

MRI is widely used to access cardiac *left ventricle* (LV) function and diagnose several heart pathologies. For instance, an important parameter used to evaluate LV function is the *ejection fraction* (EF) where the internal LV contour must be tracked during several cardiac cycles.

Usually, the physicians have to manually draw the LV contour from a stack of short-axis cine-MRI in systolic and diastolic time frames to compute the EF from these volumes. The volumes are usually composed by 10 up to 16 slices and 15 up to 30 images are acquired per cardiac cycle, corresponding to different phases of this cycle. Manually processing all this vast amount of data is time consuming and computer assistance is needed. Full automatic LV tracking and segmentation process is complex and still an open problem.

The acquired short-axis cine-MRI images present a series of obstacles that make this automatization a non-trivial problem: they are acquired over several breath-holds which can lead to the misalignment of the LV along the stack (Holland, Goldfarb and Edelman, 1998) and the signal intensity is not constant over the stack due to different sensitivity along the coil and over the slice due to cardiac flow dynamics (Pednekar, Muthupillai, Lenge, Kakadiaris and Flamm, 2006). These effects must be compensated by engaging in time consuming signal pre-processing. Therefore, a reduction of the original *field of view* (FOV) is needed to reduce the computational burden associated with the pre-processing, alignment and segmentation algorithms.

In this paper a full automatic 3D crop algorithm is proposed to select a sub-volume containing the LV in all images and in all temporal frames from the whole acquired data.

There are several semi-automatic LV segmentation algorithms described in the literature. In (Katouzian, Prakash and Konofagou, 2006) and in (Nascimento and Sanches, 2008; Nascimento and Marques, 2008) the operator must select a point in the image within the blood-pool of the LV.

Most of the proposed algorithms aiming at performing a fully automatic LV segmentation, usually follow two approaches to locate of the LV: i) they take into account the signal change over time due to muscle contraction (Cocosco, Netsch, Sénégas, Bystrov, Niessen and Viergever, 2004) or ii) they use the prior knowledge about the circular shape of the transversal cross sections of the LV (Müller, Neitmann, Merkle, Wohrle, Hombach and Kestler, 2005). Other approaches use multiple views to automatically identify the LV, such as the one proposed in (Pednekar et al., 2006).

In this work one important assumption is adopted and validated: although the heart orientation vary between exams, due to scanning protocols, the LV will never be found at the edges of the FOV and it is always close to the center of the image. The other assumptions adopted here, previously referred, are: the LV shape is circular and there is a high temporal variability of the image intensity in the myocardium boundaries. Under these assumptions, a fully automatic algorithm will be presented to calculate a ROI containing the LV.

Tests using real data have proven the robustness of the algorithm and its utility in the clinical practice.

This paper is organized as follows: Section 2 describes the image acquisition protocols and

the crop algorithm; Section 3 presents the results; Section 4 is used for discussion and main conclusions of this work.

2 Materials and method

2.1 MRI data

The presented algorithm was tested on 17 cardiac patients identified with letters from A to Q(five females and twelve males, mean age 48, ranging from 19 to 86) from *Sociedade Portuguesa de Ressonância Magnética* where the LV function was studied. The images were acquired on a 3T Philips scanner, using a Philips Sense cardiac six-channel coil. The cine-MRI study was gated to the ECG and acquired with steady state free precession image sequence. A series of 8 up to 14 short-axis slices encompassing all the LV length were acquired over 20 up to 30 time frames over the cardiac cycle. The slice thickness is of 7 mm with a 3 mm gap between them. The spacial resolution varies between 0.71 mm to 1.44 mm, normally with a value of 1.38mm, the TR/TE/flip angle varies $4.0 - 4.7/2.0 - 2.6/15^\circ - 60^\circ$, normally using values of $4.1/2.0/45^\circ$.

2.2 Algorithm description

The design of the proposed algorithm is based on the three assumptions listed in the introduction: i) the LV is close of the center of the image, ii) the LV is circular shaped and iii) there is a high temporal variability of the image intensity in the myocardium boundaries due the heart beating.

The algorithm is performed in two steps: in the first step, the center of a fixed-size predefined width ROI is estimated based on the *Hough transform* (HT) (Ballard, 1981); in the second part the center coordinates and width of the previous ROI is refined in and adaptive way.

This ROI is then extended to the entire stack of images over all the cardiac cycle frames, resulting in a 4D cropped image volume.

The algorithm was implemented in Matlab R2007b and in typical conditions spent about 2 minutes for the all processing and loading the final cropped volume.

2.2.1 Fixed-size LV windowing

Let $x(i,j,p,t)$ be the $(i,j)^{th}$ voxel in the p^{th} plane at the t^{th} time frame, where $1 < i,j,k,t < M,N,L,T$. A *standard deviation* (STD) map is computed according to Eq.2.1, using all temporal slices from the middle plane of the short-axis images stack, as displayed in the Results section in Fig.3 (b). As (Cocosco et al., 2004) suggested, high STD is found between the myocardium and the blood-pool. Additionally, this map will introduce extra ringing around the LV borders, i.e., more circular shapes. Therefore, here the *a priori* knowledge of the circular shape is used to locate the LV in the STD map using the HT.

$$STD(i,j) = \sigma_t(i,j) = \sqrt{\frac{1}{T}\sum_t \left(x\left(i,j,\frac{L}{2},t\right) - \mu_t\left(i,j,\frac{L}{2}\right)\right)^2}, \tag{2.1}$$

where $\mu_t\left(i, j, \frac{L}{2}\right)$ is the mean of the signal over the time, estimated in the position $\left(i, j, \frac{L}{2}\right)$. Before calculating the STD map, the images are filtered by a Gaussian mask to reduce the noise. This reduction is important guarantee that the STD map observed is mainly generated by temporal variations and not by spatial noise. The Canny edge detector (Canny, 1986) is then applied to get an edge-map to be used in the circular HT algorithm (see Fig. 3(c)).

The used circular HT algorithm is computed for a fixed radius and the output is an accumulator $\mathbf{Acc}$ with the same dimensions of the input image $[M, N]$. The value at $Acc_r(i, j)$ represents the number of circles with radius r centered at the edge pixels that intersect the $(i, j)^{th}$ pixel.

Based on the knowledge that the LV centroid is the center of multiple circles (the ring generated in the STD map and of the epicardial and endocardial border) and that the LV has variable size, the HT is computed for a set of different radius values. The maximum radius of the LV (at the end of the diastole) can range from 18mm to 28mm (Feigenbaum, 2005). Using this interval as reference, the HT was calculated for radius ranging from 15mm to 40mm . The maximum radius was increased to 40mm in order to include the epicardial border of the LV, and the minimum was decreased to 15mm because the middle plane of the stack might not correspond to the largest section of the LV. With steps of 2 mm of interval, the circular HT is processed for all the radius from 15mm to 40mm and the accumulators are added at each step (Eq. 2.2). The $\mathbf{Acc}_{Total}$ incorporates the whole information about circles with every radius in the range, amplifying its common center location. Adding the accumulators will ensure that the maximum will be closer to the centroid of the LV.

$$Acc_{Total}(i, j) = \sum_r Acc_r(i, j) \tag{2.2}$$

Based on the assumption that the LV is always close to the center of the image, the circles detected close to it will be favored. The $\mathbf{Acc}_{Total}$ is then multiplied by a mask that has unitary value in a circular region around the center of the image and with decreasing values up to the borders, following Eq.2.3 and showed in Fig.1.

$$h(\mathbf{x}) = \begin{cases} 1 & \text{if } \|\mathbf{x}-\mathbf{c}\| \leq R, \\ \left(\frac{1}{\|\mathbf{x}-\mathbf{c}\|} - \frac{1}{\|\mathbf{c}\|}\right) \cdot R & \text{if } \|\mathbf{x}-\mathbf{c}\| > R, \end{cases} \tag{2.3}$$

where $\mathbf{c} \in R^2$ represents the center of the image, $\mathbf{x} \in R^2$ the position of a mask element and $R = 50$mm, related with human anatomy. This value is fixed and was selected based on experimental tests and on the results from (Pednekar et al., 2006). This reference radius determines the maximum possible distance from which the LV centroid is apart from the center of the image and the circular region where the $\mathbf{Acc}_{Total}$ has unitary weight. Outside this region the $\mathbf{Acc}_{Total}$ is weighted by smaller values, reducing the importance of the detected circles in this area. The mask is zero at the corners of the image.

The new ROI is squared and centered at the coordinates of the maximum of the $\mathbf{Acc}_{Total}$. The side dimensions of this bounding box were set to $(2+\epsilon)r_{max} = 120$ mm, where $\epsilon = 1$ is a safety coefficient and $r_{max} = 40$ mm.

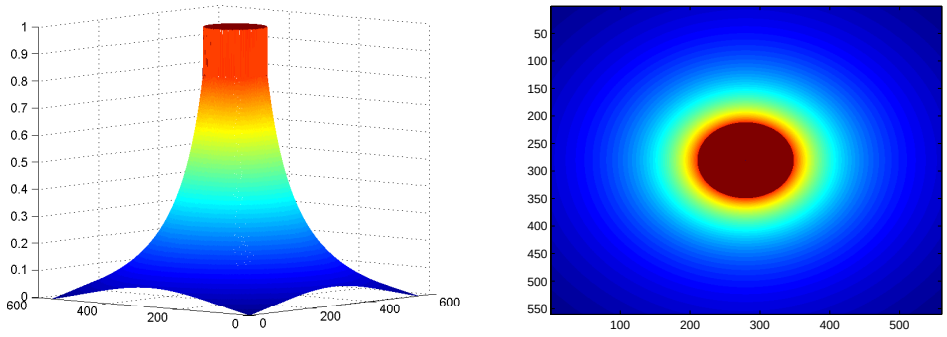

(a) (b)

Figure 1: Accumulator mask that used to reducing the importance of the detected circles outside the centered circular region. (a) 3D view (b) top view.

2.2.2 Adaptive LV windowing

In the first step of the algorithm a fixed size bounding box is generated, only depending on the pixel resolution. In the second step, the window size and center will be adapted using the previously estimated bounding box as a starting point.

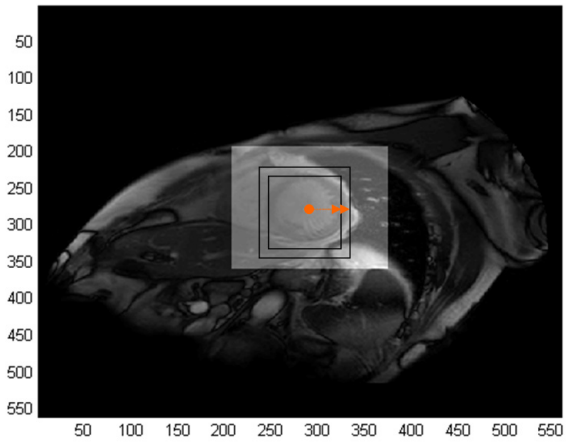

Figure 2: Growing bounding box. The orange arrows represent the direction of the increase of the side of the window.

A growing bounding box centered on the previously estimated window is used (see Fig. 2). The box size increases from $2r_{min} = 30$ mm to $3r_{max} = 120$ mm, with 10 mm gap between iterations. Let $D(k)$ be the width of the box at k^{th} step of the growing bounding box and $\mathbf{x} \in R^2$ a position in the accumulator matrix. The new parameters to generate an adaptive window are estimated by Eq. 2.4. The range of radius used in the first step is also used here. The new squared bounding box is centered at $\mathbf{c}_{adaptive}$ and with width $(2+\epsilon)r_{adaptive}$, where $\epsilon = 1$ is a safety coefficient.

$$(r, \mathbf{c})^{new}_{adaptive} = \arg\max_{r,\mathbf{x}} \mathbf{Acc}_{r,D(k)}(\mathbf{x}) \tag{2.4}$$

In Fig. 7 it is possible to observe an example of the relation between the radius and the maximum of $\mathbf{Acc}_D$ for a given D size of the growing bounding box.

3 Results

The algorithm was tunned and tested by using the images acquired from 17 patients. The R value was set to 50mm and the parameters used in Canny edge-detector are automatically selected by the algorithm. The improvements in reduction of the image size are presented in Tab. 1. The contents of the estimated bounding box for all the data-sets were visually inspected for every slice over all time frames for both steps of the algorithm.

Table 1: Size of the cropped region compared to the original image at the end of each step of the algorithm.

Patient	Fixed-Size	Adaptive $\epsilon = 1$
A	30.0%	23.0%
B	30.5%	23.4%
C	30.0%	23.0%
D	32.4%	25.6%
E	28.1%	25.3%
F	30.0%	28.4%
G	30.0%	27.9%
H	30.0%	29.5%
I	30.0%	29.5%
J	25.4%	23.7%
K	26.3%	21.5%
L	30.0%	29.5%
M	30.0%	28.9%
N	30.0%	23.0%
O	30.2%	29.7%
P	30.0%	27.3%
Q	34.0%	32.8%

All the tested data-set had successful results, *i.e.*, the LV was always within its borders (see Fig.3 as example). Although most of the data-sets presented some misalignment between consecutive planes (see. Fig. 4), the LV endocardial and epicardial borders were always inside the estimated fixed-size window.

The size of the cropped images is equal to 30.0% of the original image in most of the cases, 25.4% in the best case and 34.0% in the worst case (see Tab.1). In this step, the reduction only depends on the resolution of the image.

In Fig.3 it is possible to see an example of the results from patient Q. In the STD map it is clear the ringing effect resulting from alternating high and low STD areas due to muscle contraction and in the Canny edge-map it is possible to see circular structures in the LV region. In the

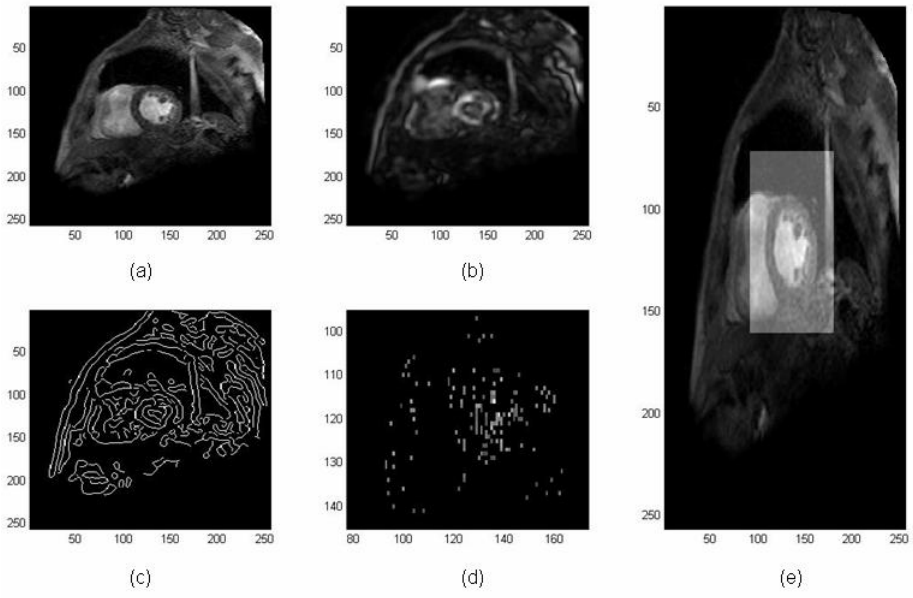

Figure 3: Results from patient Q. (a) original image (middle slice 2nd time-frame); (b) STD map; (c) Canny edge-map; (d) Filtered accumulator map, zoomed into the area where the accumulator has higher intensity; (e) Resulting bounding box highlighted in the original image.

accumulator map it is possible to identify the brighter pixel close to the LV center (around 140 in the x direction and 120 in the y direction). In the last image it is possible to observe the fixed-size window generated in the first step of the algorithm.

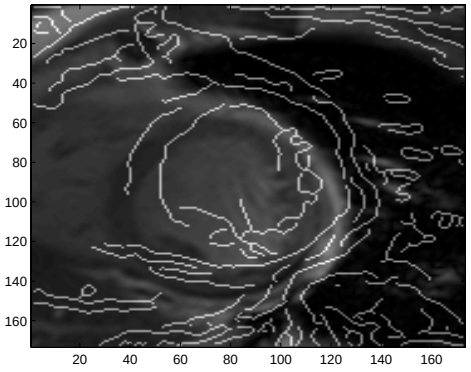

Figure 4: Misalignment between consecutive slices in the same time frame for patient A - Overlay between original bounded 4^{th} plane and bounded Canny edge-map from original 5^{th} plane

There were only two patients where the algorithm did not performed as expected. Despite the whole LV is inside the bounding box, the LV centroid is slightly away from its center (see Fig. 3).

Significantly improvements were also observed with the adaptive LV windowing, where in most the data-sets ($13/17$) the initial bounding box was reduced and centered closer to the centroid

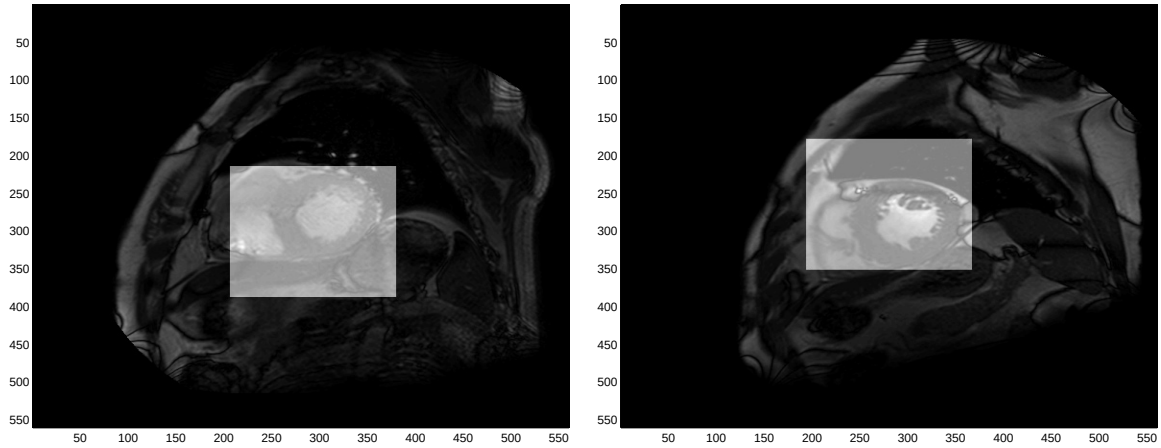

Figure 5: Not centered results. (a) Patient H (b) Patient I.

of the LV (see Fig.6). The window size was first set to $3r_{adaptive}$ where ϵ was set to 1.

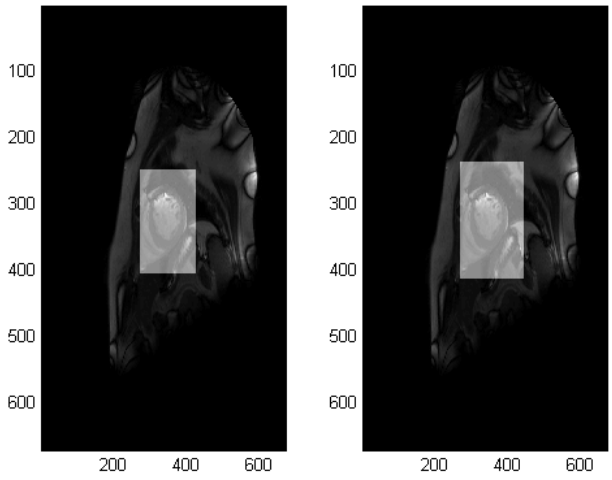

Figure 6: Windowing results from patient J (a) Adaptive LV windowing; (b) Non-adaptive LV windowing.

In the 4 unsuccessful data-sets (some examples shown in Fig. 7) the bounding box was not enough to enclose the entire LV borders. An increase of the constant factor to 3.5 eliminates this effect, but the resulting bounding box is normally slightly larger (1% to 2%) than the one from the first step of the algorithm.
In Fig. 7 it can be observed that the unsuccessful results, such as Fig. 7 (b) correspond to a sharper peak in a smaller radius in Fig. 7 (b), while the successful ones correspond to a peak for higher radius, as in Fig. 7 (a).

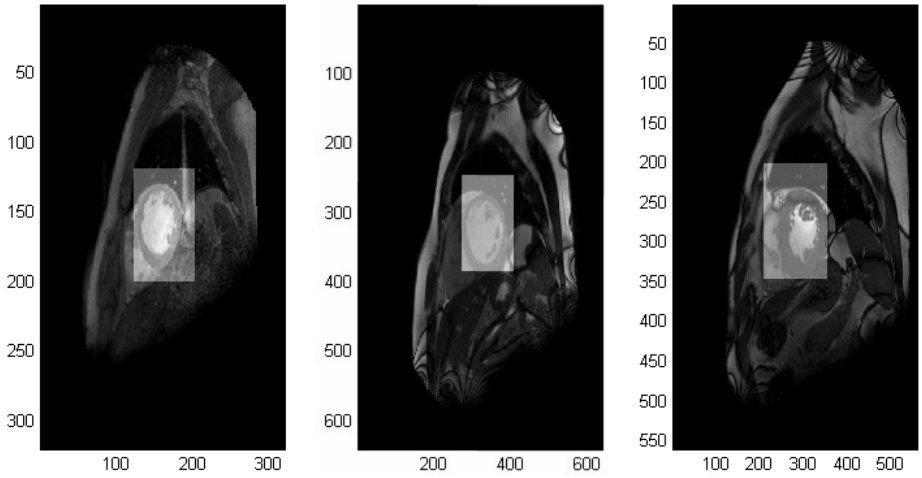

Figure 7: Thigh results from adaptive LV windowing (a) Patient E; (b) Patient K (c) Patient I.

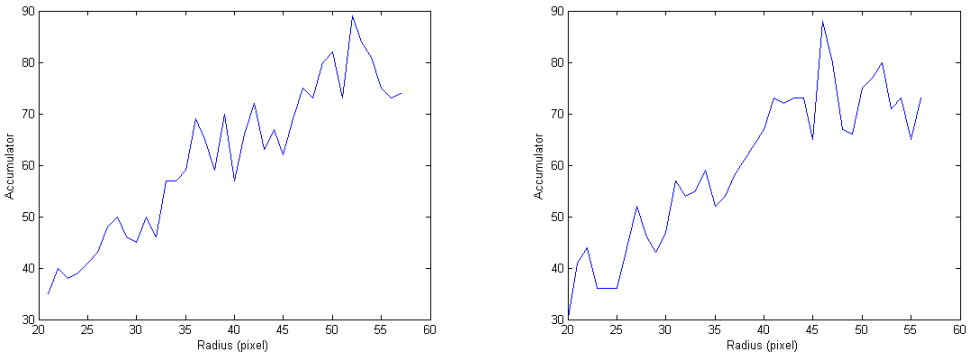

Figure 8: Graphics from biggest bounding box, radius vs accumulator. (a) Patient J (b) Patient K.

4 Discussion

LV function is assessed by using short-axis cardiac cine-MRI that represent large amounts of data: 10 up to 17 volume images over 15 up to 30 frames in the cardiac cycle. This data is inspected manually by the expert and contours are drew manually to extract the EF value. It is a time consuming process and its full automatization is of great interest.

One of the most successful method described in (Cocosco et al., 2004) is based in the high temporal variability of the image intensity in the myocardium boundaries where they are able to compute a *region of interest* (ROI) by using 79 cine cardiac structural MRI clinical scans without leaving out any part of the myocardium. The main drawback of this algorithm is to have two tunable parameters on which it depends. However, the authors were able to find some proportionality with the voxel size which makes this tunning automatic for typical adult heart dimensions.

Other approach proposed in (Müller et al., 2005) uses a size invariant circular HT (Ballard, 1981) to calculate the ROI and locate a point in the LV endocardium in a previously segmented

image. The method performed successfully for all the 31 MRI recordings. They use Otsu's method followed by a morphological operator to segment a connected region where the point calculated by the HT will fall. This method does not take into account the signal change along the slice which makes the thresholding method less robust.

The short-axis images typically have 512×512 pixels covering a FOV containing the heart and much more. Reduction of matrix dimension is an important first step to exclude unrelevant information and speed up the processing tasks.

This paper presented a fully automated crop function that successfully performed this task over the data from 17 patients.

As previously mentioned, the signal intensity is not constant over the volume due to differences in the sensitivity along the coil and also along the slice due to cardiac flow dynamics (Pednekar et al., 2006). This algorithm proved to be robust to signal variation over the image, which is usually a difficulty that must be dealt with. The proposed algorithm is able to cope with this problem because it does not depend directly on the original image but on the STD map, which decreases its sensitivity to these fluctuations and provides edge maps that contain all ringing information required for the success of the circular HT, which is robust to fragmented contours.

Furthermore, cine-MRI are acquired along several breath-holds from the patient, in order to prevent respiratory motion artifacts. This can lead the misalignment of the LV along the stack (Holland et al., 1998) if the subject is not able to hold its breath properly during each volume acquisition time slot. Although the algorithm only takes the middle slice to calculate the bounding box, it has proven to be robust to plane misalignment, mainly because they are usually small and the cropped window is big enough to fit them.

It is not, however, able to consistently locate the exact center of the LV because usually it is not a trivial task to define it. This is shown in the results from patient H and I in Fig. 3. Although the center was not located successfully, the center of the bounding box is close enough from the LV centroid. This algorithm located another circular structure close to the LV, like the myocardium that encloses the LV and the right ventricle, who's center is close to the LV.

The results obtained in the first step of the algorithm can be improved in the second step, where a window-size refinement is performed.

With a $\epsilon = 1$ it was possible to see that in a few cases the LV was not completely enclosed by the bounding box. However, in these cases a clear peak could be observed in the graphics as the ones presented in Fig. 7 (b), in opposition to most of the successful cases where the peak was located at higher radius. This peak represents a clear increase of the accumulator, identifying circular shape for a given radius, in contrast to the biased increase in the accumulator value with the increase of the radius. A proper filtering of this graphic could improve the radius selection and, therefore, a refined bounding box.

Further reduction might be possible once the images are aligned and the centroid of the LV is properly identified.

5 Conclusions

LV contour extraction and tracking is important in diagnosis of cardiac pathologies. In the clinical routine, this procedure is performed manually using software assistance, a time consuming process and presents high intra/inter operator variability. Its automatization is of great importance to the clinical practice.

The large amount of data of these cine-MRI exams requests a dimension reduction into a ROI that encloses entirely the LV over the stack and over all the time frames acquired in order to reduce the computational burden associated with the pre-processing and segmentation algorithm.

In this paper it was proposed an algorithm to automatically crop based on the well known Hough transform for circles, in the prior knowledge about the location of the heart and also on the high signal variability over time due to muscle contraction at the LV borders.

This algorithm was tested over 17 data-sets of cine-MRI from patients with cardiac pathologies where the LV function was accessed. The first step of the algorithm provided a reduction to a squared ROI with width equal to 30% of the original images. Promissing results were also achieved in the second step of the algorith, where it was possible to increase the reduction but still with a few limitations.

The performance of this algorithm was compared with state of the art algorithms ((Müller et al., 2005) and (Cocosco et al., 2004)) but there where no quantitative data available about the reduction accomplished. However, this crop algorithm seems to be more robust to the difficulties presented by these exams.

Reduction of dimension if of great importance for the tasks that follow in the segmentation of the LV: alignment and segmentation. Here is presented an automated crop procedure, which opens the door to a fully automated segmentation of the LV.

Acknowledgment

All the clinical data used for this work was supplied by Sociedade Portuguesa de Ressonância Magnética. The circular HT algorithm was implemented by (Amin, 2004).

References

Amin, S. 2004. Circular hough transform algorithm, *Photogrammetry and Computer Vision Devision, Geomatics Department,Faculty of Engineering, University of Tehran,Iran* .

Ballard, D. H. 1981. Generalizing the hough transform to detect arbitrary shapes, *Pattern Recognition* **13**(2): 111–122.

Canny, J. 1986. A computational approach to edge detection, *Pattern Analysis and Machine Intelligence, IEEE Transactions on* **PAMI-8**(6).

Cocosco, C. A., Netsch, T., Sénégas, J., Bystrov, D., Niessen, W. J. and Viergever, M. A. 2004. Automatic cardiac region-of-interest computation in cine 3d structural mri, *CARS* pp. 1126–1131.

Feigenbaum, H. 2005. *Feigenbaum's echocardiography*, PA: Lippincott, Philadelphia.

Holland, A., Goldfarb, J. and Edelman, R. 1998. Diaphragmatic and cardiac motion during suspended breathing: preliminary experience and implications for breath–hold mr imaging, *Radiology* **209**: 483–489.

Katouzian, A., Prakash, A. and Konofagou, E. 2006. A new automated technique for left- and right-ventricular segmentation in magnetic resonance imaging, *Engineering in Medicine and Biology Society, 2006. EMBS '06. 28th Annual International Conference of the IEEE* pp. 3074–3077.

Müller, A., Neitmann, A., Merkle, N., Wohrle, J., Hombach, V. and Kestler, H. 2005. Contour detection of short axis slice mr images for contraction irregularity assessment, *Computers in Cardiology* pp. 21–24.

Nascimento, J. C. and Marques, J. S. 2008. Robust Shape Tracking with Multiple Models in Ultrasound Images, *IEEE Transactions on Image Processing* **17**(3): 392–406.

Nascimento, J. and Sanches, J. 2008. Ultrasound imaging lv tracking with adaptive window size and automatic hyper-parameter estimation, *Proceedings IEEE ICIP 2008*, 2008 IEEE International Conference on Image Processing, San Diego, California, U.S.A.

Pednekar, A., Muthupillai, R., Lenge, V., Kakadiaris, I. and Flamm, S. 2006. Automatic identification of the left ventricle in cardiac cine-mr images: Dual-contrast cluster analysis and scout-geometry approaches, *Journal of Magnetic Resonance Imaging* **23**: 641–651.

Wu, K. and Lima, J. 2003. Noninvasive imaging of myocardial viability: current techniques and future developments, *Circulation Research* **93**: 1146–1158.